JOURNAL OF GEOPHYSICAL RESEARCH, VOL. 115, D10201, doi:10.1029/2009JD012517, 2010

Cloud properties and radiative forcing over the maritime storm tracks of the Southern Ocean and North Atlantic derived from A-Train

Gerald G. Mace[1]

Received 19 May 2009; revised 29 September 2009; accepted 2 December 2009; published 18 May 2010.

[1] Annually averaged cloud properties, cloud radiative effects, and cloud radiative heating from 20° × 20° latitude-longitude regions in the Southern Ocean (50°S, 135°W) and the North Atlantic (55°N, 25°W) are compared using quantities derived from measurements collected by active and passive remote sensors in the NASA A-Train. The algorithm suite used to infer cloud properties along the nadir track of the CloudSat and CALIPSO satellites takes input from the cloud boundaries from the merged active remote sensors, radar reflectivity from CloudSat, liquid water path derived from the Advanced Microwave Scanning Radiometer on Aqua, optical depth derived from the Moderate Resolution Imaging Spectroradiometer on Aqua, and top-of-atmosphere (TOA) fluxes measured by the Clouds and the Earth's Radiant Energy System. Errors in annually averaged cloud radiative effect are estimated to range from approximately 5 to 10 W m^{-2} and heating rate uncertainties range from 0.5 to 2 K day^{-1}. The study regions demonstrate a high degree of similarity in cloud occurrence statistics, in cloud properties, and in the radiative effects of the clouds. Both regions are dominated by a background state of boundary layer clouds (mean liquid water path ~150 g m^{-2}). Boundary layer clouds and cirrus (mean ice water path ~100 g m^{-2}) occurring either alone or together amount to approximately 75% of all clouds. Deeper frontal clouds amount to 10%–12% of the coverage. A strong net TOA cooling effect is partitioned between solar cooling of the surface and IR cooling of the atmosphere that is dominated by the ubiquitous boundary layer clouds. It is shown that regimes inferred according to their cloud top pressure and optical depth are often dominated by multiple hydrometeor layers and therefore defy simple classification. Because of this vertical distribution, hydrometeor-induced heating is distributed within the atmosphere in a different way than would be inferred from passive remote-sensing data considered alone.

Citation: Mace, G. G. (2010), Cloud properties and radiative forcing over the maritime storm tracks of the Southern Ocean and North Atlantic derived from A-Train, *J. Geophys. Res.*, *115*, D10201, doi:10.1029/2009JD012517.

1. Introduction

[2] Given the scarcity of global measurements of the vertical distribution of cloud macrophysical and microphysical properties, it is not surprising that uncertainties associated with cloud feedbacks remain the largest contributors to differences in model projections of climate warming [*Dufresne and Bony*, 2008]. With the exception of a few ground-based sites operated by the Atmospheric Radiation Measurement (ARM) Program [*Ackerman and Stokes*, 2003] and others, our knowledge of the vertical distribution of cloud properties has been limited to inferences from orbiting passive remote sensors. While programs such as the International Satellite Cloud Climatology Project (ISCCP) [*Rossow and Schiffer*, 1999] have provided benchmarks [e.g., *Zhang et al.*, 2005], observational constraints on the radiative influence of clouds have been limited to top-of-atmosphere (TOA) cloud radiative effects (CRE, defined as the difference, in watts per square meter, between the outgoing radiant fluxes in clear and cloudy atmospheric columns) derived from the Earth Radiation Budget Experiment (ERBE) [*Ramanathan*, 1987] and more recently by Clouds and the Earth's Radiant Energy System (CERES) [*Wielicki et al.*, 1998; *Wielicki*, 2001]. However, it has been known for more than two decades that the TOA CRE is, by itself, an insufficient constraint on cloud properties. As illustrated by *Potter and Cess* [2004], cloud properties can be rearranged in many ways to produce the observed TOA radiation budget [*Webster and Stephens*, 1981]. Indeed, reliance on time-averaged TOA–derived constraints and the resulting free-

[1]Department of Atmospheric Science, University of Utah, Salt Lake City, Utah, USA.

0148-0227/10/2009JD012517

dom to tune cloud parameters to match these constraints has resulted in the present uncertainties regarding cloud feedbacks.

[3] This issue has been highlighted by many authors, beginning with the seminal atmospheric general circulation (GCM) intercomparison studies of *Cess et al.* [1990, 1996] and including the more recent work of *Bony et al.* [2006] and *Stephens* [2005], in which issues regarding cloud feedbacks were highlighted. *Bony and Dufresne* [2005] and *Bony et al.* [2006] highlighted eastern ocean basin boundary layer clouds in the feedback puzzle, suggesting that these clouds shield the dark surface from strong solar heating while the clouds weakly cool the lower troposphere. More recently, *Sanderson et al.* [2008] used large ensembles of GCM simulations to diagnose which of a set of adjustable cloud-related quantities have the most influence on cloud feedbacks in a simple version of the Hadley Center model. While entrainment of mid-tropospheric air into deep convection ranked as the most critical adjustable parameter, the sedimentation rates of ice from the upper troposphere ranked a clear second. That such an esoteric quantity as the fall speed of ice crystals could have such a profound impact on climate simulations confirms the early and insightful work of *Senior and Mitchell* [1993], who reported a similarly large sensitivity to this parameter.

[4] GCMs show factor-of-five disparities in their sensitivities to clouds under climate change scenarios [*Soden and Held*, 2006]. These sensitivities can be decomposed into changes in the frequencies of occurrence of various cloud regimes and into changes in the properties of clouds that occur within the various regimes [e.g., *Bony et al.*, 2004]. *Williams and Tselioudis* [2007] analyzed output from several GCMs and found that much of the disparity in GCM climate sensitivity arises from a lack of ability of the models to represent the state of the present-day cloud radiative effect. Their finding is consistent with the results of *Potter and Cess* [2004]. Williams and Tselioudis showed that not only do the models fail to produce the frequencies of occurrence of various cloud regimes derived from ISCCP, but the radiative effects of the regimes are substantially different from observations, suggesting that the disparity in cloud feedbacks found in climate change scenarios arise not only from a failure to represent the changes in clouds as the climate warms, but also from a failure to properly represent clouds in the present climate. Therefore, what measurements must provide are additional global constraints on the vertical distribution of cloud properties, the CRE at the surface and TOA, and the vertical distribution of cloud radiative heating (CRH, defined as heating rates, in kelvins per unit of time, due to clouds).

[5] Measurements of the vertical distribution of cloud properties have become available from the 94 GHz Cloud Profiling Radar (CPR) [*Im et al.*, 2006] on CloudSat and the optical lidar on CALIPSO [*Winker et al.*, 2007]. These platforms joined the A-Train constellation of satellites [*Stephens et al.*, 2002] in mid 2006 and added critical active remote-sensing capabilities to a suite of passive sensors on several other satellites. The A-Train sensors operate across the electromagnetic spectrum from the microwave to the ultraviolet and provide an entirely unprecedented level of measurement synergy. In this study, we make an initial exploration of the capabilities of this synergy and describe the annual statistics of hydrometeor occurrence, CRE, and CRH as functions of layer top height and layer thickness in two regions of the maritime middle-latitude storm tracks.

2. Analysis Methodology

[6] The locations of hydrometeor layers are determined from CloudSat and CALIPSO using algorithms described by *Marchand et al.* [2008] and *Vaughn et al.* [2004], respectively. The hydrometeor layers from the two instruments are combined as described by *Mace et al.* [2009]. The CloudSat mask makes no attempt to discriminate between precipitating and nonprecipitating columns. Because of the nature of the radar measurement, it is impossible to determine the cloud base of a layer from which precipitation-sized particles are falling. Therefore, the bases of such layers are very uncertain.

[7] The methodology we use to derive the microphysical and radiative properties is adapted from *Mace et al.* (2006a; hereafter M06), who addressed an identical set of analysis goals with similar data. Results from the M06 methodology, including an estimate of uncertainties, are described by *Mace et al.* [2006b] and *Mace and Benson* [2008]. Here, we focus on aspects of the methodology that are unique to the present analysis of the A-Train data. It is important to distinguish the experimental algorithms and associated results presented here from the operational and official microphysical [*Austin et al.*, 2009; R. Austin and G. Stephens, Improved retrieval of stratus cloud microphysical parameters using millimeter-wave radar and visible optical depth: 1. Algorithm and synthetic analysis, submitted to *Journal of Geophysical Research*, 2008] and radiative flux [*L'Ecuyer et al.*, 2008] products from the CloudSat project.

[8] The vertical profile of microphysical properties must be estimated with algorithms that take the remote-sensing measurements as input. It is useful to examine the scope of this problem. In the most general case, a volume element in a vertical column could contain liquid and ice phases whose particle size distributions (PSD) could be composed of PSD modes that include both cloud and precipitation particles. Assuming that each of the PSD modes can be described by some mathematical function such as a modified gamma with three independent parameters, the generalized problem contains 12 unknowns. This complexity can be reduced where only a single phase is physically possible. However, it is often difficult to empirically discount the possibility that PSDs are not multimodal (e.g., drizzling stratocumulus). We focus on this issue because not only are the remote sensors sensitive to it, but also the effects of the clouds on the heat and water budgets are largely defined by the detailed properties of the microphysical profiles. So, it seems unreasonable to reduce a priori the dimensionality of the problem beyond some characterization of two modes per phase for each cloudy volume in a vertical profile. This argument must also consider other uncertainties such as the ice crystal habit, which strongly influences the cross-sectional area and mass of individual particles [*Mitchell*, 1996] and therefore the properties of particle ensembles.

[9] This discussion illustrates a degree of complexity that exists in nature that explains why the cloud feedback problem has remained illusive to observations even as passive radiometry in space and data analysis techniques have

Table 1. Description of the Four Basic Vertical Profile Types Used in the Retrieval of Cloud Properties, the Temperature Ranges for Which Each Is Applied, the Data Used for the Retrievals, the Main Assumptions, and the References for the Techniques[a]

Column Type Assumed	Temperature Range (K)	Input Data, Day	Input Data, Night	Algorithm Assumptions	Reference
Liquid only	$T > 273$	*Ze*, τ	*Ze*, LWP	Modified gamma distribution	Appendix A (day); *Dong and Mace* [2003] (night)
Mixed	$243 < T < 273$	*Ze*, LWP, τ	*Ze*, LWP	Empirical *Ze* relationship	*Mace et al.* [2006a]
Ice	$T < 243$	*Ze*, τ	*Ze*	Modified gamma distribution, *Mitchell* (1996) empirical relations	Appendix A (day); *Protat et al.* [2007] (night)
Ice over liquid	$T > 273$ and $T < 243$	*Ze*, LWP, τ	*Ze*, LWP	Empirical algorithms	*Mace et al.* [2006a], *Dong and Mace* [2003], *Protat et al.* [2007]

[a]Error is described in the text and in appendix C. Abbreviation is as follows: LWP, liquid water path.

improved. With the dimensionality of the problem exceeding the available measurements by a large degree, what can be known from passive measurements is exceedingly limited and has provided little, if any, actual constraint to the climate modeling community, as evidenced by continuing uncertainties [*Dufresne and Bony*, 2008].

[10] With the A-Train, in addition to the active instruments, other available quantities represent properties of the column in a vertically integrated sense such as liquid water path from the Advanced Microwave Scanning Radiometer on Aqua (AMSR-E) [*Wentz and Meissner*, 2000] and visible optical depth and infrared emissivity from the Moderate Resolution Imaging Spectroradiometer (MODIS) [*Platnick et al.*, 2003]. The CERES instrument measures the broadband upwelling radiances in the infrared and solar bands, and these broadband radiances are converted into fluxes [*Wielicki et al.*, 1998]. However, the problem remains severely underconstrained. Therefore, using the characteristics of the vertical column that include the vertical location of hydrometeor layers, temperature profile, number of layers, and the time of day, in this study we make decisions as to which of a set of relatively simple cloud property retrieval algorithms to apply in a given situation. We use four basic classifications that are determined broadly by the characteristics of the profile (Table 1). A column that contains only hydrometeor layers that exist at temperatures greater than freezing is classified as liquid, while profiles with layers at temperatures colder than 243 K are classified as ice. Profiles with hydrometeor layers that exist either completely or partially between these two temperature extremes are treated as if they could contain mixed phases, and columns that contain multiple layers where each layer is of a single phase (based on temperature) such as cirrus over cumulus are classified as such.

[11] We derive the microphysical properties in a resolution volume using various combinations of the radar reflectivity, the radar-lidar hydrometeor boundaries, the MODIS optical depth, and the AMSR-E liquid water path. However, not all measurements are used in every column. For single-phase layers when optical depths from MODIS are available (daytime), we apply a simple algorithm that allows for an approximate characterization of PSD bimodality (appendix A). At night, the *Dong and Mace* [2003] algorithm is applied to liquid layers to estimate the vertical profile of liquid water content (LWC) and effective radius using the radar reflectivity factor (Z) and liquid water path (LWP) from AMSR-E. At night, ice-phase layer properties are estimated using a Z-ice water content-temperature regression algorithm [*Protat et al.*, 2007]. At night, the effective radii of ice-phase layers are specified within a physically reasonable range using radiative closure with CERES, although this approach provides information only for optically thin layers. Profiles that contain multiple layers are considered by using the radar reflectivity, the MODIS optical depth (during day), and the AMSR-E LWP in the nighttime algorithm set. Finally, for layers that are potentially of mixed phase, we use the empirical approach described in M06.

[12] There are typically several physically reasonable choices that can be made when prescribing empirical relationships and assumptions. These include, for instance, the exponents of the assumed modified gamma distributions (i.e., appendix A and Figure A1). These choices change the microphysics enough to change the calculated TOA radiative fluxes by a modest amount. Therefore, radiative closure with CERES fluxes at the TOA is used as a means to iterate between a finite set of physically reasonable empirical relationships in any given set of profiles within a CERES footprint. Because the footprint of CERES is 20 km, the use of CERES data for radiative closure is complicated by the variability of clouds below the CERES resolution. The simple iterative technique applies an independent column approximation assumption to the profile types described in Table 1. Appendix B describes the iterative scheme in more detail, and uncertainties are discussed in appendix C.

3. Evaluation of Retrieved Microphysics

[13] Many of the issues regarding the uncertainties of the basic methodology and several of the algorithms are addressed in M06 and *Zhang and Mace* [2006]. Appendix C of this study also discusses uncertainty in retrieved microphysics and the derived radiative effects. In this section, we focus on comparing the algorithm results to observations collected in situ for cirrus and from ground-based observations for liquid-phase clouds. We also compare the present retrieved cloud properties with other retrievals, including those from MODIS, AMSR-E, and operational cloud products released by the CloudSat science team.

3.1. Field Program Comparisons

[14] The NASA-funded Tropical Composition, Clouds and Climate Coupling experiment (TC4) was based in San Jose, Costa Rica, during July and August 2007. We focus

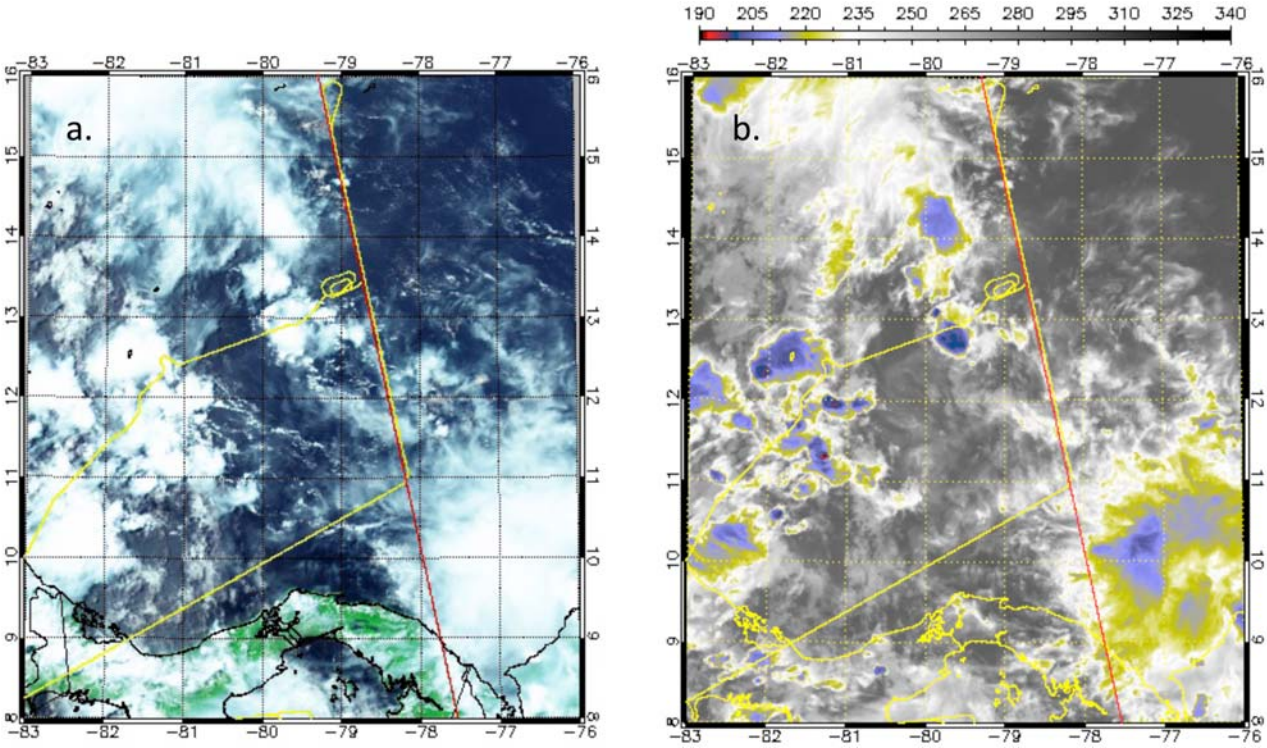

Figure 1. The 22 July 2007 case study. (a, b) Three-color composite visible and IR (color in brightness temperature in Kelvin units) Moderate Resolution Imaging Spectroradiometer (MODIS) imagery showing the CloudSat/CALIPSO track (red) and the track of the NASA DC-8 (yellow). (c) The CloudSat radar reflectivity. (d) CALIPSO attenuated backscatter. (e) The radar-lidar geometrical profile mask created by combining the CloudSat and CALIPSO data.

initially on a DC-8 flight segment from July 22. This several hundred kilometer track penetrated an optically thin cirrus layer that was at least 24 h removed from a deep convective source based on visual inspection of satellite imagery (Figure 1). We compare ice water content (IWC) derived from the CERES-constrained Z-τ algorithm with measurements of IWC from the counterflow virtual impactor (CVI) [*Twohy et al.*, 1997] and the two-dimensional stereo probe (2DS) [*Lawson et al.*, 2006] from which water contents are calculated using the approach described by *Lawson and Baker* [2006] (Figure 2). The IWC results shown here are calculated using the flux closure technique described in appendix B. The effects of iterating to radiative closure have been tested with this case. Using the default quantities for the exponents in the assumed PSD function of $\alpha = -1.0$ and $\beta = 3.0$ (see appendix A for details) yielded correlation between the CVI and Z-τ retrieval of $\log_{10}$(IWC) of 0.45. With iteration using the exponent pairs in Figure A1a with CERES solar flux as an additional constraint, this correlation increased to 0.52.

[15] The agreement between the Z-τ results and the data collected on the DC-8 is strongest during the early portion of the track, when the cirrus layer was most uniform, and during the later portion of the track, which corresponded to the time of the overpass at approximately 1845 UTC near 15.5°N. Substantial disagreement between the measurements and the retrievals can be seen between 12.8°N and 13.5°N. The peak in IWC observed by the DC-8 instruments at 12.8°N had apparently translated slightly along track by the time CloudSat passed over 23 min after the DC-8. While the 2DS observed breaks in the cloud field following this spike, the CVI continued to record IWC. This discrepancy is likely to be due to a known hysteresis issue in the CVI. Along this portion of the track where the 2DS found breaks in the cloud field, CloudSat observed cirrus. It is unknown whether this difference is due to advection or development of the cloud field during the intervening minutes or whether cirrus existed elsewhere in the 1 km wide and 500 m deep resolution volume of the radar.

[16] Figure 2 also illustrates the relatively good agreement in the extinction derived from the 2DS PSD and the extinction derived using the approach described in appendix A, where the layer-averaged extinctions derived from MODIS optical depths and the CloudSat-Calipso cloud boundaries are distributed vertically using a $Z^{0.58}$ weighting [*Matrosov et al.*, 2003]. Figure 2 also compares other observed and derived quantities with the present algorithm. The CERES solar fluxes shown in Figure 2c have been used to constrain the retrieval (appendix B). The variability in the cloud field that exists at scales smaller than the 20 km CERES footprint documented by the higher-resolution A-train measurements is evident. Figure 2e shows that, because the algorithm uses a variational technique, the derived optical depth results do not identically agree with the input MODIS optical depths because we allow for error in the input values. The comparison of water path in Figure 2d shows reasonable agreement

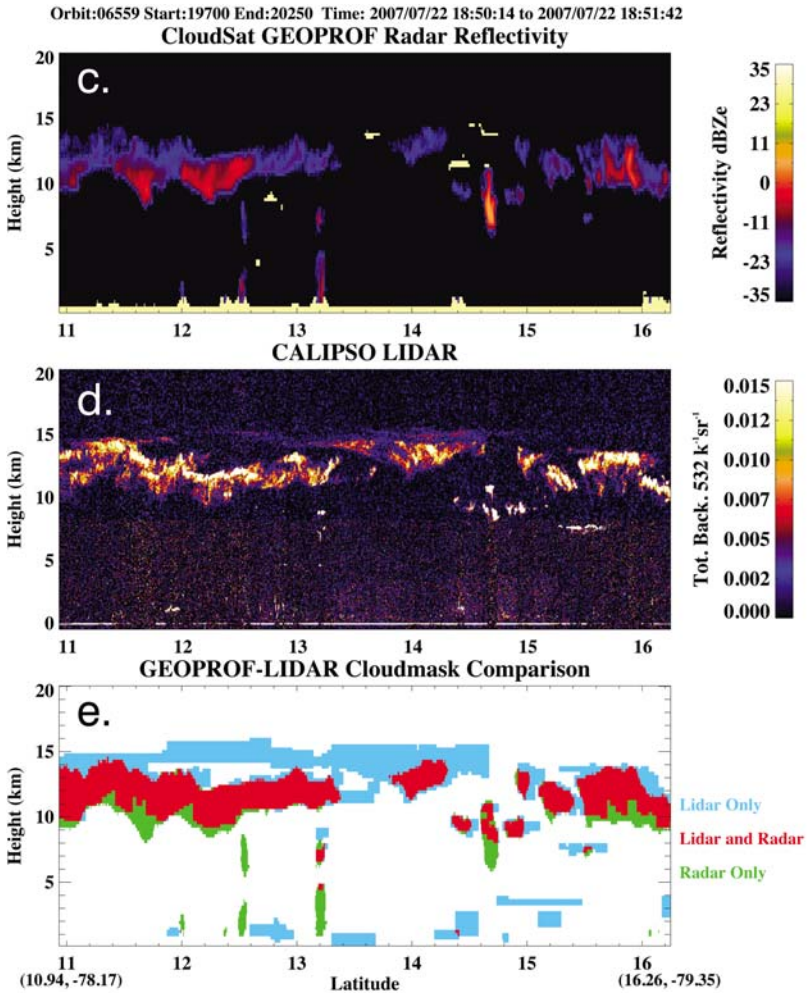

Figure 1. (continued)

between the Z-τ algorithm and the technique described by *Platnick et al.* [2003] that is applied to MODIS. Since the τ in the Z-τ algorithm is also derived from MODIS, the comparison is not entirely independent. For additional discussion of uncertainty in the derived quantities see *Zhang and Mace* [2006], M06, and appendix C.

[17] The DC-8 collected data along the CloudSat-CALIPSO track on 29 July, 3 August, and 9 August. These tracks were shorter than the track on 22 July and were in thicker anvil cirrus compared to July 22. We quantify the correspondence between the retrievals and the measurements in Figure 3 and Table 2 using the four underflights of the A-Train by the DC-8 during TC4. While there is a relatively high correlation between the measurements and retrievals, comparison of the Z-τ results with aircraft demonstrate large scatter, with RMS between 60% and 70%. The retrievals seem to be biased lower than the measurements, with a median difference of −18%. The normal deviation, which is defined as the RMS difference of the retrievals about a linear regression line fitted to the comparison, are on the order of 10 mg m^{-3}, which is just slightly smaller than the mean value of the measurements. The retrievals that use only radar reflectivity demonstrate a larger bias and poorer correlation, demonstrating the importance of synergy in the A-Train measurements.

[18] The retrieval problem is more straightforward for liquid-phase layers since the empirical relationships describing mass and cross-sectional area of condensate reduce to those appropriate for spheres. The iteration scheme described in appendix B chooses among the three sets of exponents listed in Figure A1b that are appropriate for bimodal and unimodal distributions. The Z-τ algorithm when applied to liquid layers is primarily applicable to stratocumulus or shallow cumulus that is not heavily precipitating because we do not account for attenuation by liquid water and non-Rayleigh effects in the transfer of radar energy through the cloud layer, although attenuation by water vapor and oxygen in the vertical profile is accounted for in the retrieval algorithm.

[19] No correlative data in maritime stratocumulus are available that we can use for validation of the algorithm as we did for cirrus. Therefore, we use data collected at the Southern Great Plains (SGP) ARM site. The radar reflectivity at the ARM site is collected by the millimeter cloud radar (MMCR) [*Clothiaux et al.*, 1999], and the optical depths are

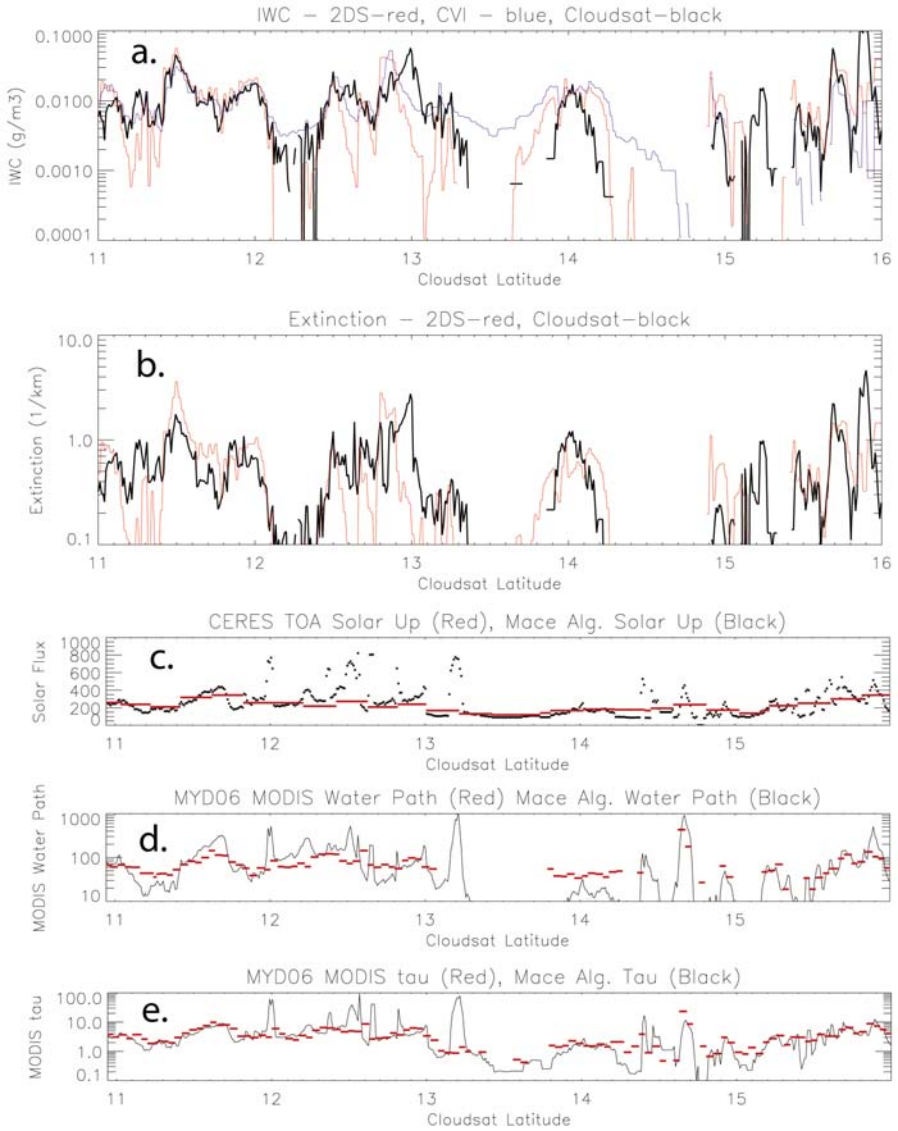

Figure 2. Comparison of cirrus cloud properties retrieved along the DC-8 track shown in Figure 1 with observed and retrieved quantities. (a) Extinction calculated using the retrieved PSD with extinction derived from measured particle size distributions (PSD) using the two-dimensional stereo probe (2DS) instrument. (b) Ice water content (IWC) derived using retrieved PSD with measurements of IWC by the counterflow virtual impactor (CVI) and 2DS on the DC-8. (c) Comparison of top-of-atmosphere (TOA) upwelling solar fluxes from retrieved cloud properties with measurements by Clouds and the Earth's Radiant Energy System (CERES). (d) Comparison of retrieved ice water path (IWP) with IWP retrieved using the MYD06 algorithm. (e) Comparison of visible optical depth of retrieved PSD with optical depth derived using MODIS reflectances.

derived from measurements of the multifilter rotating shadowband radiometer (MFRSR) using the algorithm described by *Min and Harrison* [1996]. To test the algorithm, we isolate several boundary layer stratus events that took place at SGP. We then implement the Z-τ algorithm as we would for A-Train data using the three α and β pairs listed in Figure A.1b and choose the exponent pair that provides the best agreement in MWR-derived LWP (Figure 4). This iteration is similar to the iteration that we apply when comparing to CERES fluxes as described in appendix B. We find that we are often able to identify an exponent pair that provides a reasonable diagnosis of the MWR LWP. Overall the procedure results in good accuracy and minimal bias in LWP. However, it is not known if a different set of exponents would prove more optimal in other cloud regimes such as the maritime regions examined in this study. Additional field data will be analyzed as they become available.

3.2. Comparison to Other Retrieval Results

[20] Science teams in support of A-Train instruments have been developing cloud property retrievals for many years. These include the MODIS atmosphere team, who retrieve the

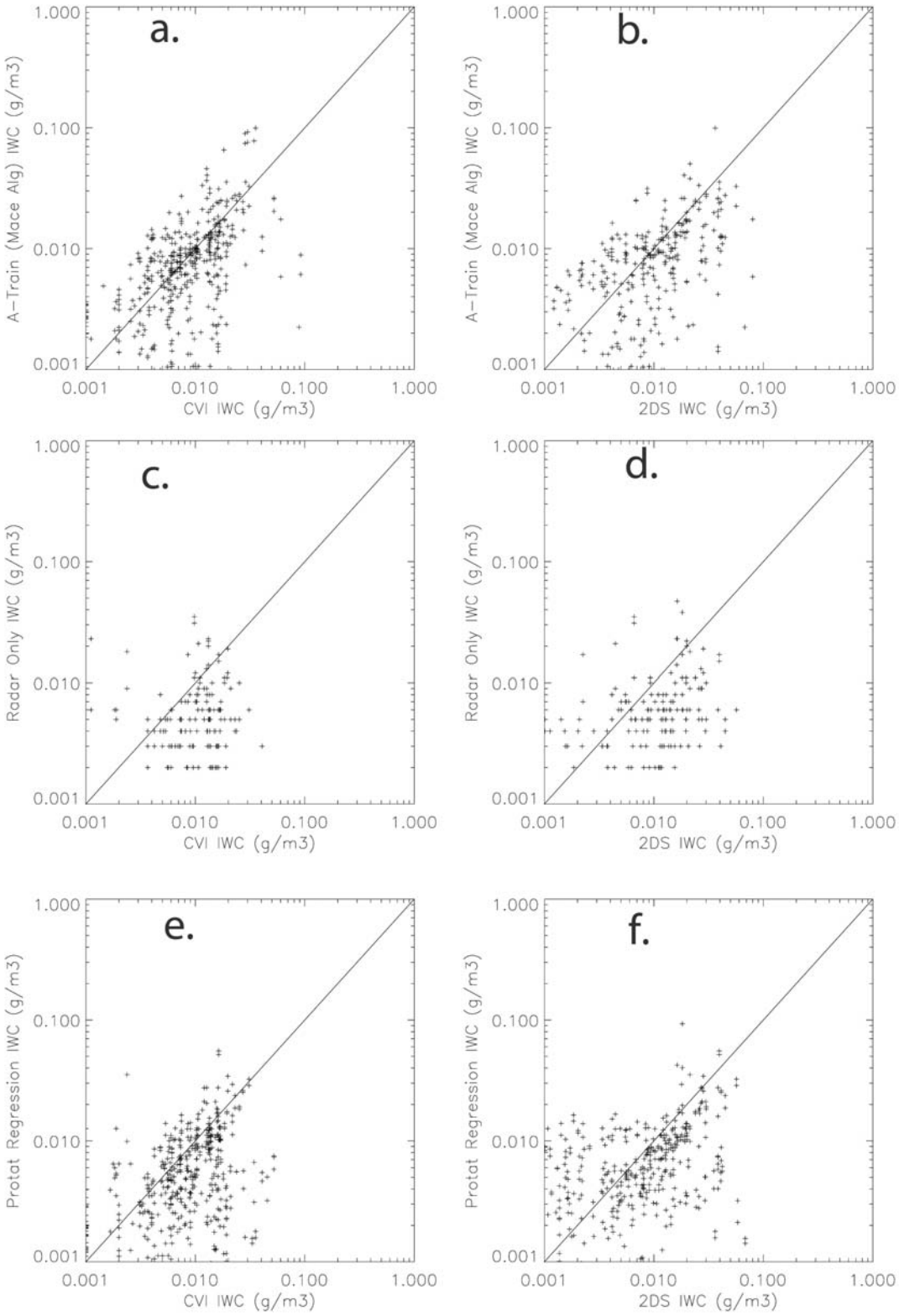

Figure 3. Comparison of A-Train–retrieved cloud properties with cloud properties observed by instruments on the NASA DC-8 during the 2007 Tropical Composition, Clouds and Climate Coupling campaign during underflights of CloudSat and CALIPSO on 22 July, 29 July, and 3 August. (right) Results using CVI IWC measured from the DC-8. (left) Results using IWC derived from the 2DS probe on the DC-8. (a, b) Comparison of properties retrieved using algorithms described in this study. (c, d) Comparison of properties retrieved using the CloudSat radar-only algorithm. (e, f) Comparison with the *Protat et al.* [2007] regression algorithm.

Table 2. Summary of Various Algorithm Results Compared to in Situ Data Collected by the NASA DC-8 During the Tropical Composition, Clouds and Climate Coupling Experiment[a]

Algorithm	Measurement	RMS Error (Fraction)	Mean Absolute Difference	Normal Deviation	Correlation Coefficient
Z-τ ice	CVI IWC	0.61	−0.18	0.009 g m^{-3}	0.75
	2DS IWC	0.70	−0.18	0.010 g m^{-3}	0.72
	2DS extinction	0.75	−0.15	0.51 km^{-1}	0.73
CloudSat radar-only	CVI IWC	0.90	−0.55	0.010 g m^{-3}	0.55
	2DS IWC	1.02	−0.55	0.012 g m^{-3}	0.36
Protat et al. [2007] regression	CVI IWC	0.81	−0.55	0.009 g m^{-3}	0.54
	2DS IWC	0.99	−0.45	0.008 g m^{-3}	0.47
Z-τ *liquid*	ARM MWR	0.40	−0.03	128 g m^{-3}	0.79

[a]See also Figure 3. Abbreviations are as follows: ARM, Atmospheric Radiation Measurement Program; 2DS, two-dimensional stereo probe; CVI, counterflow virtual impactor; IWC, ice water content; MWR, microwave radiometer.

liquid and ice water path and column-averaged effective radius using MODIS data ([*Platnick et al.*, 2003]; hereafter referred to as the MYD06 product) and the AMSR-E team, who derive cloud liquid water path from the passive microwave measurements [*Odell et al.*, 2008]. Recent comparisons of these products are encouraging [*Borg and Bennartz*, 2007]. The CloudSat project has also released an official cloud microphysical product that includes the ice and liquid water content profiles retrieved globally based on radar reflectivity ([*Austin et al.*, 2009; Austin and Stephens, submitted manuscript, 2008], hereafter referred to collectively as the CloudSat radar-only or RO product).

[21] Figures 5a–5i show comparisons of liquid and ice water paths derived using the techniques described in the appendices and the previous section (hereafter referred to as the M10 results) with MYD06, AMSR-E, and RO. The comparisons are derived from data collected during the month of January 2007 in the 20° × 20° regions shown in Figure 6. The footprint sizes of these instruments differ significantly. MYD06 has a 5 km resolution, AMSR-E has an approximately 20 km resolution, and M10 has an approximately 2 km resolution. The plots in Figure 5 show nearest-neighbor matches to the M10 footprints. We also averaged the M10 results within the footprints of the other measure-

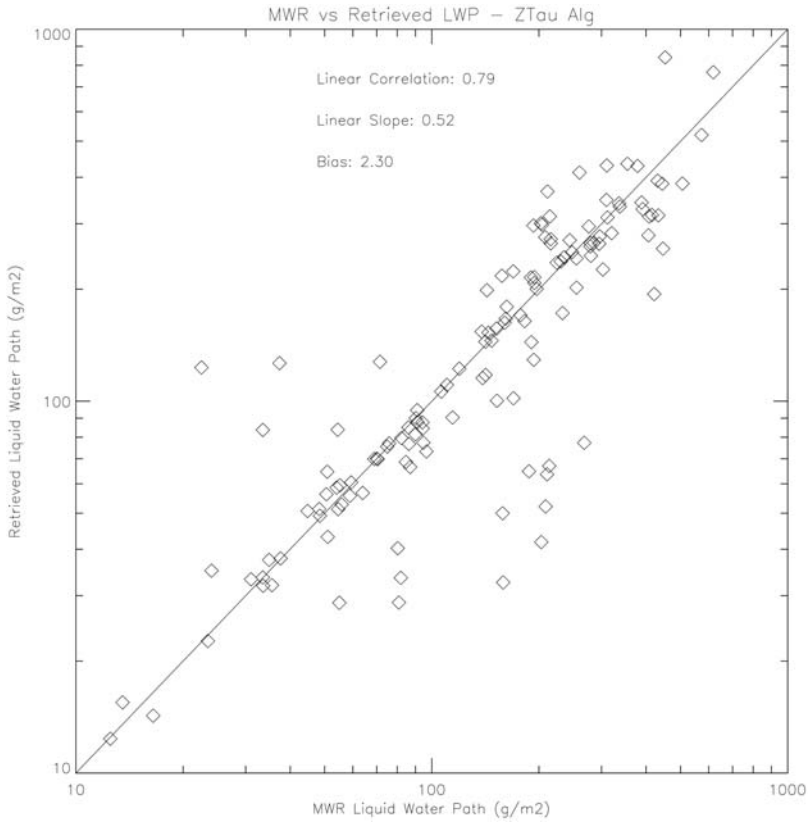

Figure 4. Comparison of liquid water path retrieved using the Z-τ algorithm described in appendix A applied to millimeter cloud radar data and optical depths retrieved from the multifilter rotating shadowband radiometer using the algorithm of *Min and Harrison* [1996] with liquid water paths derived from microwave radiometer (MWR) data.

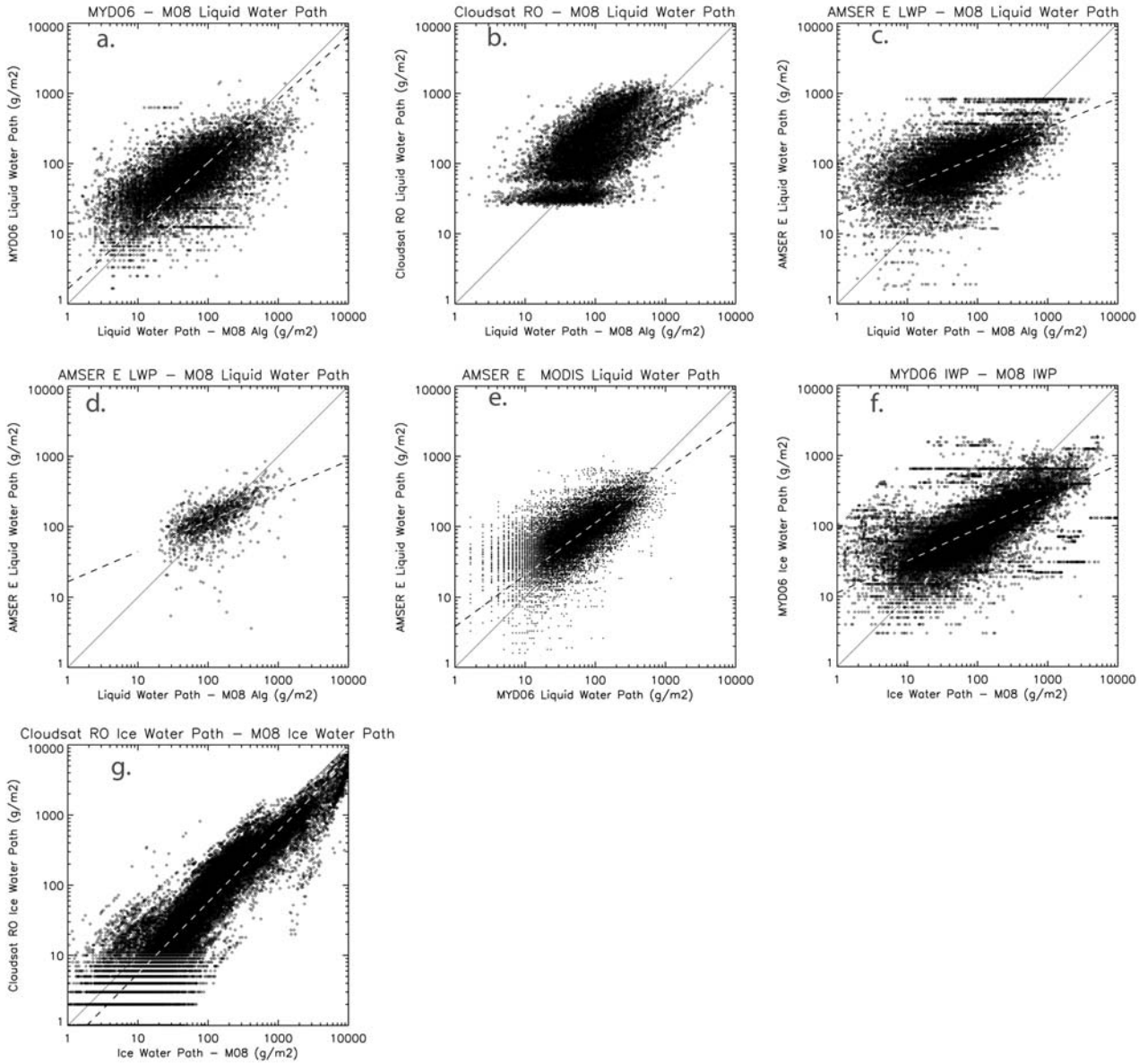

Figure 5. Comparison of cloud properties and radiative quantities derived from or observed by the A-Train sensors from the analysis regions shown in Figure 6 during the month of January 2007. The quantities compared and the sources of the data are described in the title of each image, and the units are shown on the axis labels. AMSR-E LWP, the official retrieval product produced by the Advanced Microwave Scanning Radiometer–EOS team; M10, the set of algorithms described in this study in the text and in appendices A and B; MYD06, the official Aqua-MODIS cloud product produced by the MODIS atmosphere team; RO, version 4 of the official CloudSat radar-only product. Additional details of the comparisons are described in the text.

ments using different filtering criteria to test the impact of partial cloudiness. While in some cases these exercises reduced the scatter slightly, the qualitative nature of the results shown in Figure 5 did not change.

[22] In the interest of full disclosure it is helpful to indicate the relationships between the various derived quantities compared in Figure 5. Of course the M10 algorithm and the RO algorithms both use CloudSat-observed Z and the description of the layer locations in that data set. Beyond this, the algorithmic approaches are not related. The MYD06 and the M10 results use MODIS reflectances in some way, although the algorithm [*Polonsky et al.*, 2008] used to derive the optical depth used in the Z-τ retrieval is independent of the MYD06 algorithm. The M10 LWP results compared with the AMSR-E retrievals shown in Figure 5 are derived using the Z-τ CERES flux-constrained algorithm and *do not* use AMSR-E data as input.

[23] For vertical columns that unambiguously consist of liquid-only cloud layers (Figures 5a–5c with statistics summarized in Table 3 for selected comparisons), the best

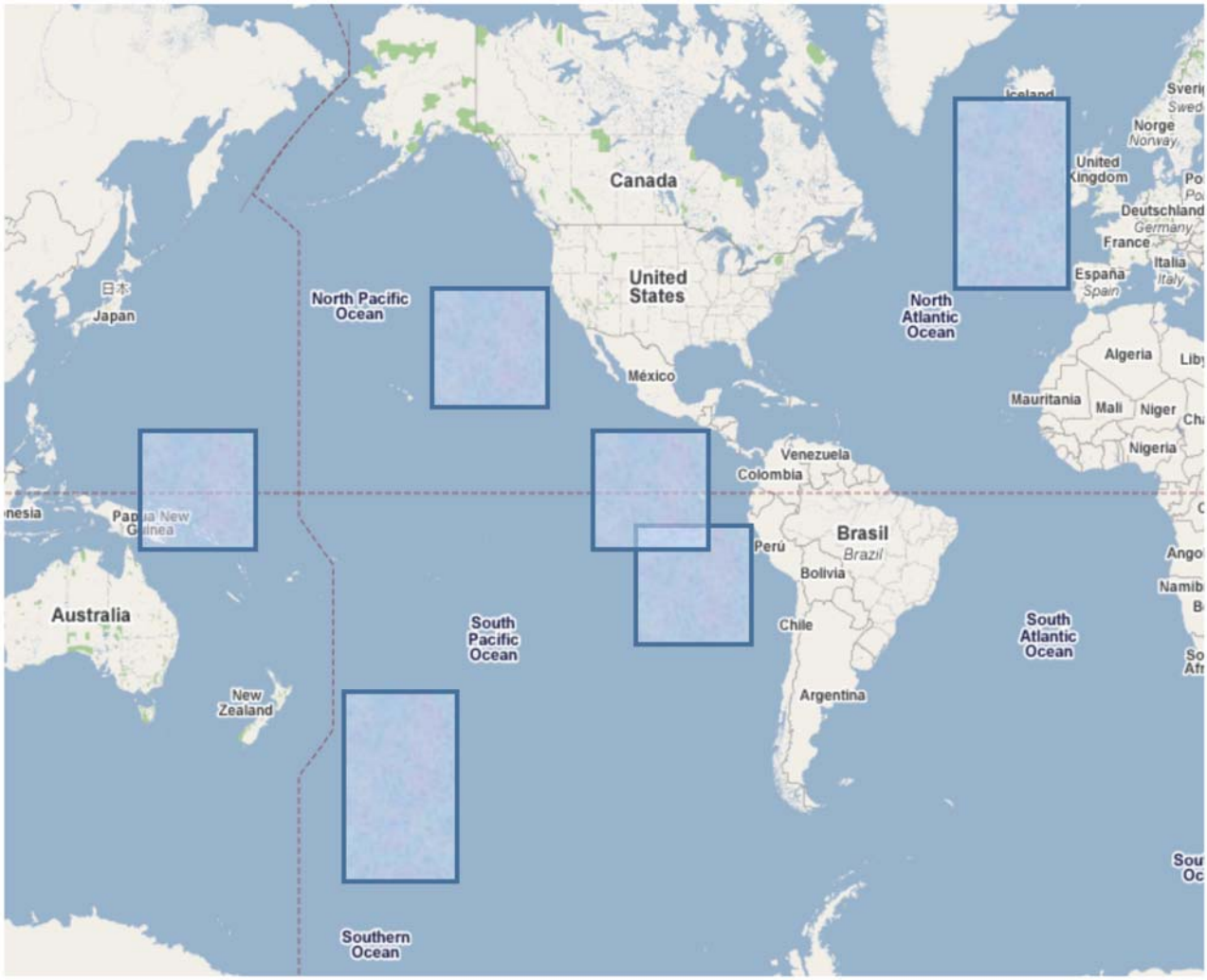

Figure 6. Analysis regions to which the algorithms described in this study are applied. The scatterplots in Figure 5 use data derived from all of these regions. Cloud properties and radiative quantities from the Southern Ocean and North Atlantic study regions are described in detail.

agreement between M10 and MYD06 is found after application of the 0.83 correction factor [*Wood and Hartmann*, 2006] to the MYD06 LWP values. The agreement between M10 and MYD06 liquid water paths in Figure 5a is expected since optical depths derived from MODIS radiances are used as input to the boundary layer cloud algorithms used to derive the M10 results (appendix A). This agreement suggests a similar level of agreement in the layer mean effective particle sizes inferred from the two algorithms. The linear regression between M10 and MYD06 in Figure 5a falls nearly on the 1:1 line, whereas in Figure 5c, while a reasonably strong correspondence is found, the slope of the regres-

Table 3. Comparison of Algorithm Results Derived from the Techniques Described in This Study With Similar Quantities Derived From Other A-Train Sensors[a]

Column Type	Product Compared to M10	RMS Difference (Fraction)	Mean Absolute Difference (Fraction)	Normal Deviation (g m^{-2})	Correlation coefficient
Liquid	MYD06	0.82	+0.17	71	0.55
	RO	1.25	+0.87	206	0.48
	AMSR-E	1.1	+0.88	86	0.55
Ice	MYD06	0.69	−0.02	130	0.62
	RO	0.85	−0.4	240	0.92

[a]Abbreviations are as follows: AMSR-E LWP, the official retrieval product produced by the Advanced Microwave Scanning Radiometer–EOS team; M10, the set of algorithms described in this study in the text and in appendices A and B; MYD06, the official Aqua-MODIS cloud product produced by the MODIS atmosphere team; RO, version 4 of the official CloudSat radar-only product.

sion line is much shallower than found in Figure 5a. Figure 5d shows the results of averaging the M10 results within the AMSRE-E footprints and requiring all CloudSat footprints within an AMSR-E footprint to be diagnosed with a LWP of >20 g m^{-2}. Those requirements significantly reduce the number of comparison points, but the overall statistics of the comparison is similar. Figure 5e compares MYD06 and AMSR-E results at the pixel level, where systematic differences are seen at lower values of LWP. *Greenwald et al.* [2007], in analyzing pixel-level data, also found systematic discrepancies in the AMSR-E and MYD06 LWP retrievals for lower LWP amounts. These biases were a function of various environmental properties that influence the upwelling microwave energy such as surface wind speed and partial cloudiness. *Borg and Bennartz* [2007] found no such disagreement between AMSR-E and MYD06 when averaging in 1° × 1° regions on monthly time scales. Their technique tends to smooth discrepancies that are derived from partially filled volumes and sensitivity issues. Rather poor agreement is found between M10 and the RO results (Figure 5b). While some linear correspondence is noted, the bias is substantial. This result is not surprising since the RO algorithm uses no additional information other than radar reflectivity. It is well known that Z poorly constrains the properties of marine boundary layer clouds because of their propensity to drizzle.

[24] Figures 5f and 5g compare the ice water path (IWP) from MYD06 and RO with the M10 results. These comparisons include only those profiles that appear, based on their temperature, to be composed only of ice and have no lower layers. The comparison with MYD06 is highly correlated but with a shallow slope in the regression line. In essence, the MYD06 results agree most strongly with the M10 retrievals when IWP is between 20 and 100 g m^{-2}. Below about 20 g m^{-2}, MYD06 is higher than M10, while above 100 g m^{-2}, the MYD06 values are lower. This tendency can be seen as well in the 22 July TC4 results (Figure 2d). The reasons for this behavior are not known; however, differences in assumed particle habit and size distribution shape between the two algorithms perhaps contribute [*Mace et al.*, 2005]. Unlike the LWP comparison, the comparison between RO and M10 shows a much stronger agreement over nearly the entire range of retrieved values. We do note a low-RO bias, however, of approximately 30% that is consistent with the TC4 comparison (Figure 3).

4. Results: Southern Ocean and North Atlantic Study Regions

[25] We exploit the synergy of the A-Train measurements to examine and compare the statistics of cloud occurrence, cloud microphysics, and cloud radiative heating over 20° × 20° latitude-longitude regions centered over the Southern Ocean and North Atlantic storm tracks (Figure 6). From a global energy balance standpoint, the role of the storm systems that characterize the poleward reaches of the middle latitudes is to remove, via transports of sensible and latent heat, excess energy from equatorial and subtropical regions and deposit that energy at the poles. The upward vertical motions associated with these storms as they progress through their life cycles produce copious clouds and precipitation. Indeed one of the most characteristic features of Earth when viewed from space is the existence of cyclonically curved frontal cloud systems that extend over the maritime regions of the middle latitudes in both hemispheres. The radiative effects of middle-latitude cloud systems have been examined in many important papers, including the seminal studies that used the early Earth Radiation Budget Experiment (ERBE) data collected in the late 1980s [e.g., *Ramanathan*, 1987] and the series of papers (e.g., *Rossow and Zhang*, 1995; *Zhang and Rossow*, 1997; *Chen et al.*, 2000) that examined the International Satellite Cloud Project data sets [*Rossow and Schiffer*, 1999]. These studies demonstrate that the TOA radiative impact of the cloud systems in the storm tracks seasonally reverses sign, with the high albedo dominating a net cooling influence during summer, while IR warming becomes more predominant during winter, when sun angles are low. These TOA radiative effects counter the latitudinal temperature gradients and thereby dampen the baroclinic storms, requiring, ultimately, the storms to become deeper and/or more numerous to accomplish the energy transports [*Weaver*, 2003].

[26] An interesting and often unappreciated aspect of the cloud climatology of these regions is that the deep frontal clouds comprise a relatively small fraction of the total cloud cover over any particular location during an annual cycle. The cloud climatology of these regions is dominated by a background state that is composed primarily of geometrically thin boundary layer clouds that range in character from stable stratus that forms in poleward flows where warm air moves over relatively colder waters to vast sheets of cumulus and stratocumulus that change character from open cellular in regions of strong cold air advection to closed cells in regions of free tropospheric subsidence [*Norris and Iacobellis*, 2005]. The predominance of the boundary layer clouds causes annual cloud cover to exceed 80% in both study regions [*Mace et al.*, 2009]. This predominance of low-level cloud clover is also evident in the vertical distribution of cloud occurrence shown in Figure 7. The vertical distributions show that upper tropospheric and boundary layer clouds predominate, while a relatively lower hydrometeor occurrence is found in the middle troposphere. Notable also is the similarity of the vertical distributions in the two study regions. Except for a larger peak in the low-level maximum over the Southern Ocean, the two vertical distributions are nearly identical.

[27] Above 10 km, the majority of the cloud layers are quite tenuous, representing primarily radar reflectivities below −25 dBZ_e. Below 10 km, higher reflectivities become more prominent, with nearly one third of all radar returns reporting radar reflectivities in excess of 0 dBZ_e below 5 km. In the analysis that follows, we present cloud property and radiative forcing statistics in terms of the maximum radar reflectivity found in a profile. As discussed in appendix A and by *Mace et al.* (2006a), the algorithms that we apply do not specifically treat precipitation. A more thorough treatment of attenuation by absorption of the radar energy by liquid water would be required, as would a full treatment of non-Rayleigh scattering and even multiple scattering in heavier precipitation and thick clouds. The +10 dBZ_e threshold effectively filters profiles that include melting layers and underlying rain. The 0 dBZ_e threshold excludes nearly all light rain and most drizzle as well as most snowfall. Therefore, in addition to presenting cloud properties for all data irrespective of the dBZ_e max-

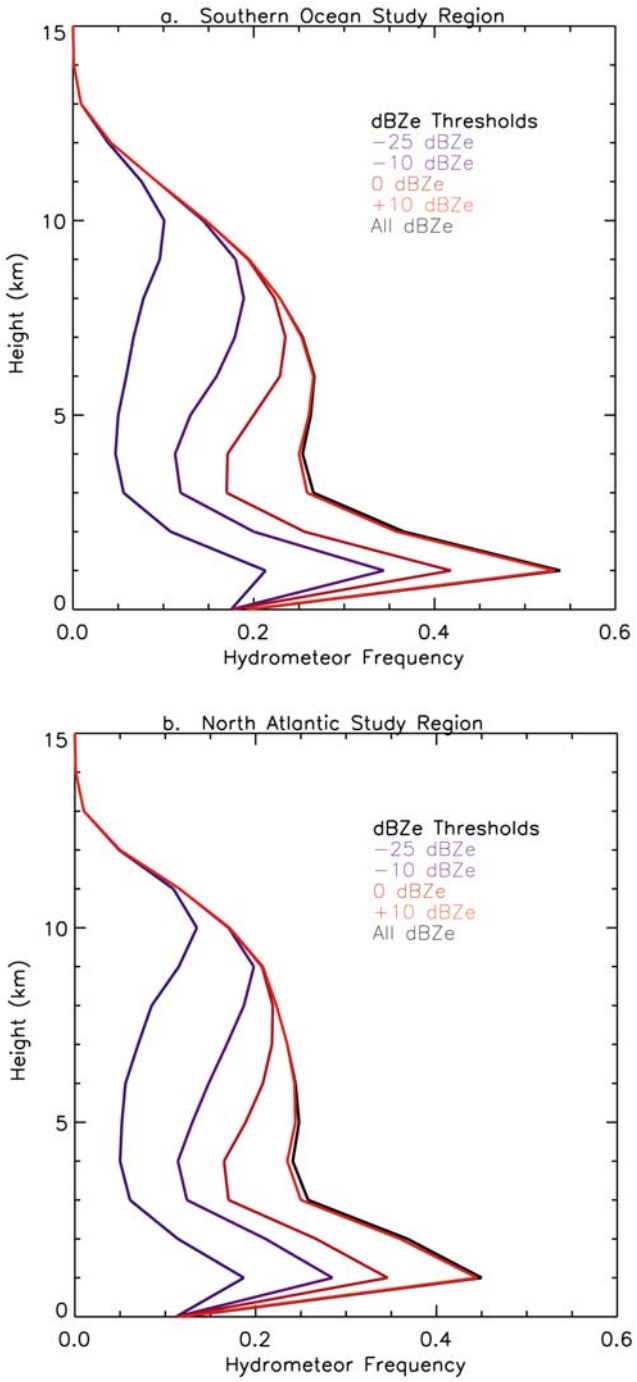

Figure 7. Frequency of hydrometeor occurrence in 1 km vertical bins in the CloudSat-CALIPSO merged data set collected during calendar year 2007 in the 20° × 20° regions centered at (a) 50°S, 135°W (Southern Ocean) and (b) 55°N, 20°W (North Atlantic). The radar reflectivity thresholds indicate the occurrence frequency for all observations that have radar reflectivity below the threshold value.

imum in the profile, we also present statistics for dBZ_e maxima of −10 and 0. Figure 7 shows that a +10 dBZ_e maximum would remove only a small fraction of the data, while a 0 dBZ_e maximum would tend to remove approximately 25%–30% of the data.

[28] Given the similarities in the vertical profiles of radar reflectivity between the two study regions, it is not surprising that the frequency distributions (FDs) of liquid and ice water paths and the liquid and ice effective radii compiled from all cloudy profiles are statistically indistinguishable between the two study regions (Figures 8 and 9 and Table 4). The effect on the statistics of filtering based on the profile maximum radar reflectivity is illustrated in Figure 9. Fundamentally, the extreme values in the FDs are removed, while their overall characteristics remain unchanged. To test the similarity in these FDs we used the Wilcoxon rank sum test [*Wilcoxon*, 1945], which determines the similarity between two FDs that are not necessarily Gaussian. A hypothesis that the distributions are drawn from a similar population is assumed, and we mark with an asterisk in this and in following figures the quantities where that hypothesis can be rejected at the 95% confidence level. The liquid water path FD in this semilog space is somewhat skewed to smaller quantities, with modal values in the FD near the mean values between 130 and 150 g m^{-2}. The ice water path FDs are dominated by thin ice cloud layers, with mean values ranging between 25 and 30 g m^{-2}. The general shape of the distributions is similar to that of cirrus FDs compiled from ground-based climatologies [e.g., *Mace et al.*, 1998; *Comstock et al.*, 2002]. The effective radii of the liquid layers are strongly skewed and show a modal value between 5 and 10 μm with a median effective radius of 12 μm. The ice layers are more normally distributed, with mean and median values ranging between 20 and 40 μm.

[29] Given the strong similarities in cloud properties, differences in radiative effects of the cloudy layers (CRE) are also fairly small between the North Atlantic and Southern Ocean. From a TOA perspective, clouds in these study regions have a strong net cooling influence on the column, with values of −51 and −38 W m^{-2} over the Southern Ocean and North Atlantic, respectively. Even with these large mean differences, the distributions of TOA CRE are statistically indistinguishable. Note that the standard deviations over both regions are on the order of 150 W m^{-2} and are determined largely by the highly skewed solar CRE.

[30] The TOA CRE values agree reasonably well with quantities published from analyses of ERBE, ISCCP, and CERES. *Kim and Ramanathan* [2008] present the most recent analysis of global solar CRE. From their Figure 10b, we find annually averaged solar CRE in the −70 to −80 W m^{-2} range over these oceanic regions, with the North Atlantic study region having a value larger by about 10 W m^{-2} than the Southern Ocean region. Their 3 year imagery-based analysis is certainly more statistically sound than our single year of vertical curtain measurements, and we must also recall that our daytime measurements take place near solar noon. This temporal aspect would tend to bias our results high relative to a true daily average. On the other hand, the highly skewed nature of the FDs in Figures 8 and 9 do call into question the meaningfulness of the regional mean quantities derived from them. This issue is illustrated nicely by *Rossow and Zhang* [1995], who present January and July as well as annually averaged CRE. They show over this latitude range that the monthly averaged net CRE varies from −150 W m^{-2} during summer over the Southern Ocean to values greater than zero on a monthly average during winter. In the infrared, our results at the TOA range between +40 and +45 W m^{-2}, with

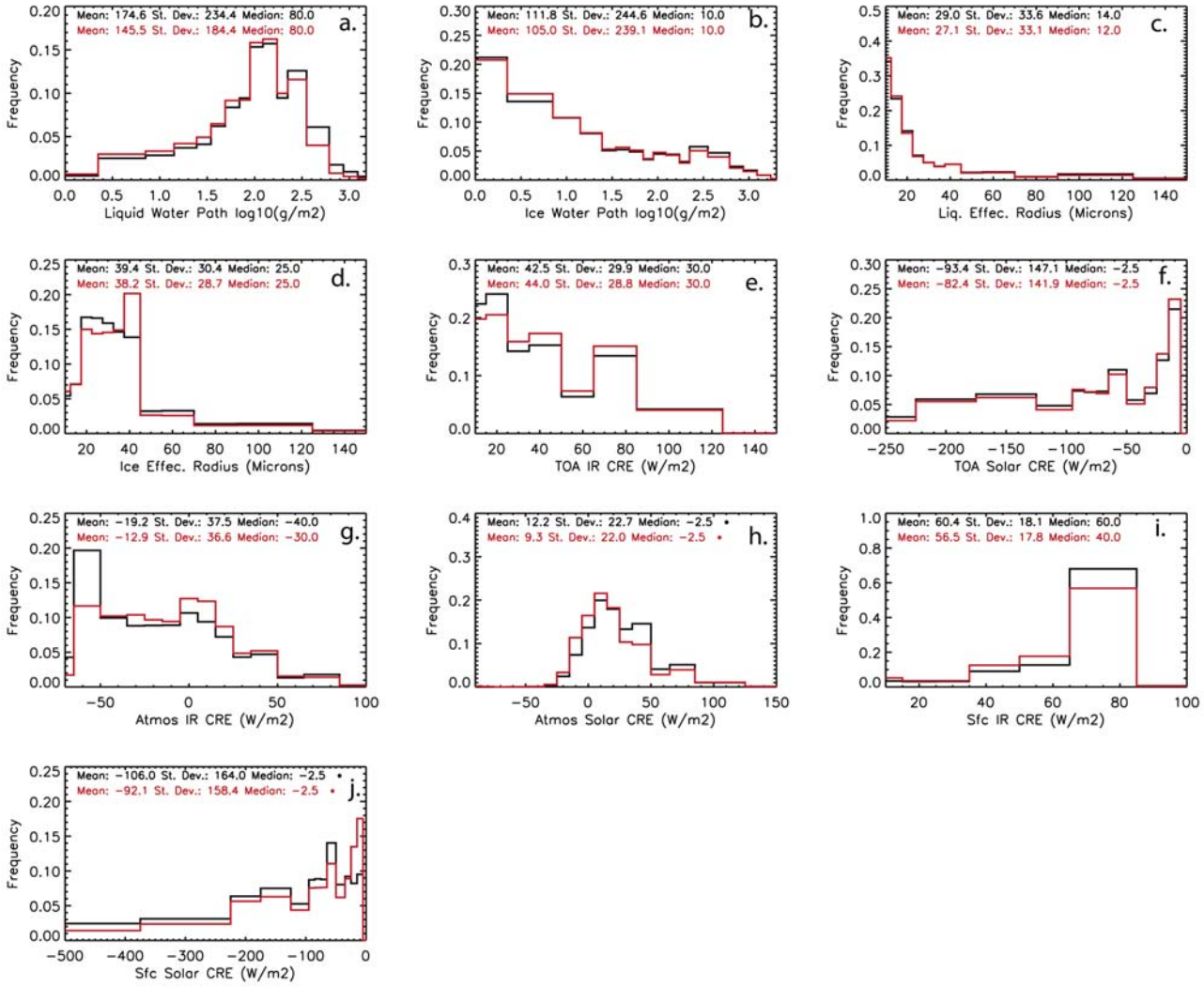

Figure 8. Frequency distributions of cloud and radiative properties over the Southern Ocean (black) and North Atlantic (red) study regions (Figure 6) composed from all cloudy profiles collected during the 12 month period from January to December 2007. The frequency distributions were calculated from profiles whose maximum radar reflectivity was less than 10 dBZ_e to avoid uncertainties regarding precipitation. Approximately 400,000 profiles were analyzed from each region. (a–d) Liquid and ice water paths and the vertically averaged liquid and ice effective radii. (e–j) The solar and infrared cloud radiative effects at the top of atmosphere (TOA), within the atmosphere (ATM), and at the surface (Sfc).

standard deviations of approximately 30 W m^{-2}, and are in good agreement with the statistics reported by *Ramanathan* [1987].

[31] The partitioning of the TOA CRE between the atmosphere and surface is quite dependent on which spectral band is considered. The solar CRE is largely realized as cooling at the ocean surface. Even coupled with an approximately 60 W m^{-2} of IR warming at the surface, clouds exert between 20 and 30 W m^{-2} of net annually averaged cooling because of the strong predominance of the solar albedo effect (this net cooling would be smaller for a true diurnal cycle). In the atmosphere, the situation is strikingly different. The FD of IR CRE in the atmosphere, while negative overall with means between −13 and −19 W m^{-2}, arises from a broad distribution, producing a standard deviation of 37 W m^{-2}. As we show below, the IR heating and cooling are strongly dependent on cloud type. We find that solar heating largely counterbalances the IR cooling in the atmosphere. This finding of near cancellation of solar and IR CRE in the atmosphere was also reported by *Mace and Benson* [2008], who analyzed 8 years of ground-based data collected at the Oklahoma ARM site using a similar set of retrieval algorithms as used here. This result is in disagreement with *Rossow and Zhang* [1995], who found that the atmospheric solar CRE have mean values near zero. *Stephens* [2005] argued, based on the ISCCP findings, that clouds simply redistribute vertically the clear-sky solar heating that would otherwise occur. Because the solar heating and cooling changes imposed by clouds are partially the result of how the clouds modify the passage of solar radiation through atmospheric water vapor and condensed water in the

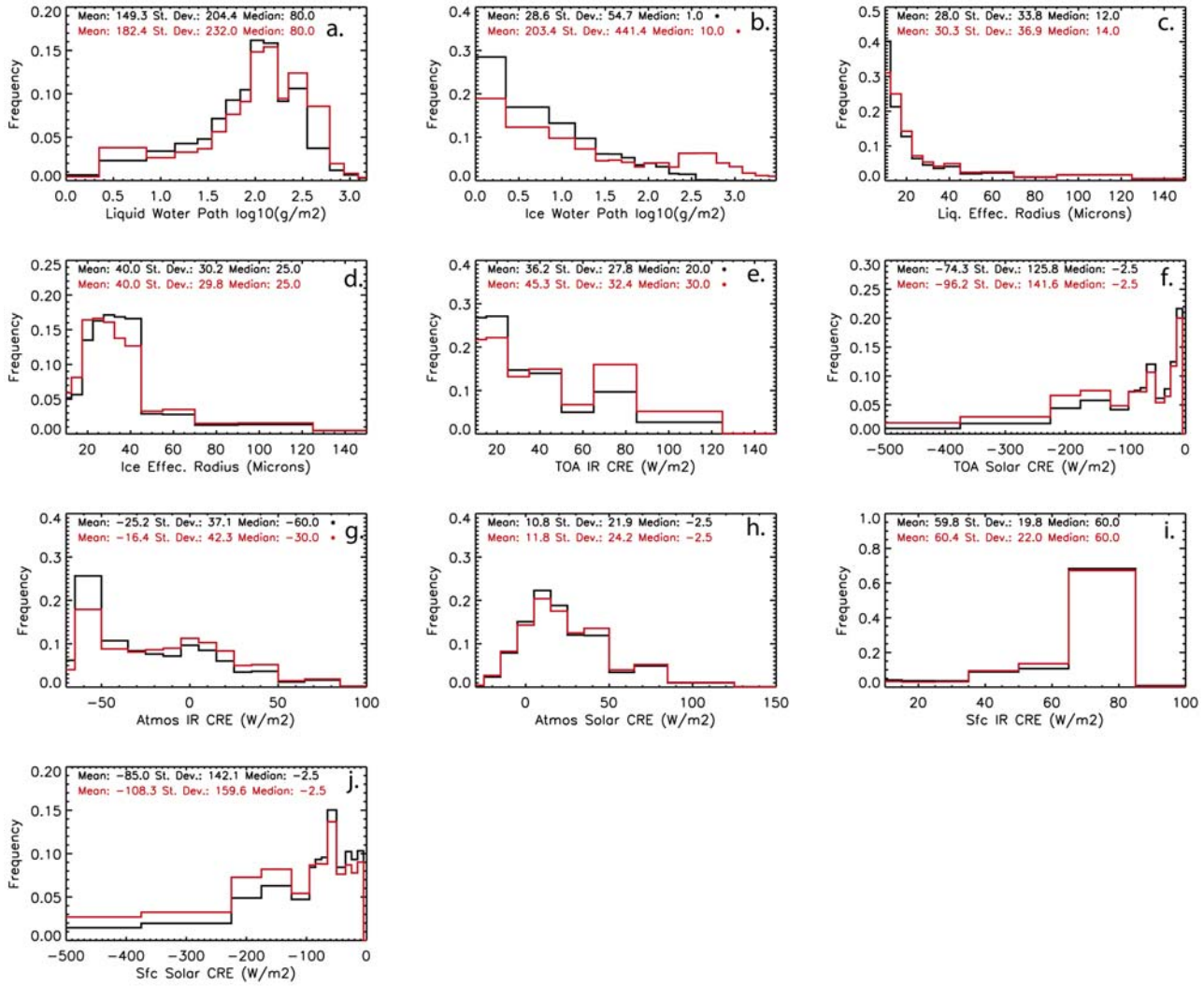

Figure 9. As in Figure 8, except that statistics from only the Southern Ocean study region are shown. The red curves are compiled from all data irrespective of the maximum reflectivity in the vertical profiles, and the black curves are compiled by excluding any profiles that have reflectivity greater than 0 dBZ_e.

lower troposphere, the magnitude and even sign of cloud-induced heating depend on the vertical distribution of cloud properties.

[32] Until the advent of active cloud remote sensing in space, our understanding of the vertical distribution of hydrometeor layer properties and their radiative forcing is derived primarily from statistical analysis of results from ISCCP and related techniques. By necessity much of the literature exploring this topic has conformed with the ISCCP diagnostic convention that consists of 42 cloud top pressure (CTP) and visible optical depth (τ) bins that are often reduced to nine specific classifications: three cloud top height classes that roughly correspond to the traditional low, middle, and high cloud classes and three τ classes that range from what would be considered optically thin to very opaque [*Ockert-Bell and Hartmann*, 1992]. Our understanding of the distribution of clouds on Earth has been largely defined within this context [e.g., *Bony et al.*, 2006], and the fidelity of models is often judged by their ability to match ISCCP statistics [e.g., *Zhang et al.*, 2005]. Because vertical layer structure information has been missing, it has been difficult to interpret statistics derived from these regimes. Figures 10 and 11 classify the annual A-Train results in the study regions in terms of the ISCCP classifications. Shown are the relative frequencies of the classes, the statistics of the column mean water paths, and radiative forcing quantities. Mean heating rate profiles are also shown.

[33] Overall, the primary differences in these results between the two study regions are in the relative frequencies of occurrence of the cloud classes. The North Atlantic region shows relatively more of the thin and moderately thick high cloud classes than does the Southern Ocean. The Southern Ocean then makes up for this in a higher frequency of occurrence of thin and moderately thick boundary layer clouds. Both regimes demonstrate an identical frequency of thick, high-topped layers that likely represent frontal regimes. Identical frequencies of middle tropospheric classes are also found between the study regions. Otherwise, the properties of hydrometeor layers, their radiative effects, and their heating profiles are nearly identical between the two

Table 4. Cloud and Radiative Effect Statistics Compiled for All Cloudy Columns with the Specified Maximum Radar Reflectivity Upper Threshold Over the Study Regions in Figure 6 During the Calendar Year 2007[a]

	$dBZ_e < 0$			$dBZ_e <+10$			All dBZ_e		
	Mean	STD	Median	Mean	STD	Median	Mean	STD	Median
Ice Water Path (g m^{-2})									
NA	28	57	5	105	240	10	195	455	10
SO	29	55	1	112	245	10	203	441	15
Liquid water path (g m^{-2})									
NA	132	182	80	146	184	80	158	197	80
SO	149	204	80	175	234	80	182	232	80
r_e Liquid (μm)									
NA	25	33	12	27	33	12	27	34	14
SO	18	18	10	29	34	14	27	33	14
r_e Ice (μm)									
NA	38	30	25	38	29	25	39	30	25
SO	40	30	30	39	30	25	40	32	25
Top-of-the Atmosphere Solar Cloud Radiative Effect (W m^{-2})									
NA	−75	121	−2.5	−82	142	−2.5	−91	145	−2.5
SO	−74	126	−2.5	−93	147	−2.5	−96	151	−2.5
Top-of-the-Atmosphere IR Cloud Radiative Effect (W m^{-2})									
NA	38	27	20	44	29	30	46	30	30
SO	36	28	20	43	30	30	45	31	30
Within-the-Atmosphere Solar Cloud Radiative Effect (W m^{-2})									
NA	10	21	−2.5	9	22	−2.5	10	22	−2.5
SO	11	22	−2.5	12	23	−2.5	12	23	−2.5
Top-of-the-Atmosphere IR Cloud Radiative Effect (W m^{-2})									
NA	−18	36	−40	−13	37	−30	−11	37	−30
SO	−25	37	−60	−19	38	−40	−16	38	−20
Surface Solar Cloud Radiative Effect (W m^{-2})									
NA	−86	137	−2.5	−92	158	−2.5	−102	161	−2.5
SO	−85	142	−2.5	−106	164	−2.5	−108	168	−2.5
Surface IR Cloud Radiative Effect (W m^{-2})									
NA	55	20	40	57	18	60	57	17	40
SO	60	20	60	60	18	40	60	18	60

[a]dBZ_e values indicate the radar reflectivity threshold. Uncertainties of the quantities vary as described in the text and in appendix C. Abbreviations are as follows: NA, North Atlantic; SO, Southern Ocean.

regions. This similarity is no surprise, given that the classification criteria largely define the column radiative properties and, thereby, the radiative effects. In general, we find that the water paths and the radiative forcing increase from the thin to thick optical depth classes, with the high clouds heating the atmosphere by a magnitude that is only weakly dependent on total optical depth, although the heating profile becomes an increasingly strong function of height, with a large degree of cancellation between heating in the lower and cooling in the upper troposphere as the column optical depth increases with the total water path. Low-level clouds are a significant source of strong lower tropospheric cooling, while middle-level clouds have a largely neutral effect on the total column heating, although significant vertical structure in the heating profile can be seen that, like the high clouds, is a strong function of column optical depth.

[34] It is interesting to note how the vertical distributions of hydrometeors change as a function of column optical depth within the middle and upper tropospheric classes. These classes are typically thought of in terms of their cloud tops. For instance, the classes with tops less than 440 hPa are considered to be composed of high clouds, and the 440–680 hPa classes are thought of as mid level. This assumption appears to be approximately true only in the optically thinnest bins. The intermediate and thick classes (especially for high clouds) demonstrate a strong bimodal vertical frequency distribution, with low-level clouds being as prevalent as high clouds. These occurrence frequencies are generated by distinct multiple layers of high clouds over low clouds, as demonstrated in Figure 12. The optically thin middle and high clouds, while having a small amount of low-level clouds, are predominantly composed of clouds within the upper and middle troposphere. Distinct layers that exist almost entirely in the boundary layer appear in the intermediate and optically thick classes. Given the similarities in the ice and liquid water paths of the intermediate and optically thick high cloud classes, it would seem that as much of the column optical depth is as due to thicker liquid clouds as due to thicker ice clouds.

[35] The studies of *Rossow and Zhang* [1995] and *Chen et al.* [2000] use the ISCCP convention of placing a single-layer cloud with a particle size of 10 μm of the derived optical depth at the diagnosed cloud top pressure to compute the radiative effect of the layer. *Chen et al.* [2000] present zonal averages of radiative forcing quantities derived from 4 days of data collected in January. Comparison of the Southern Ocean results in Figure 10 with the zonal average of *Chen et al.* [2000] is interesting. In general, the IR CRE that we find is larger at the TOA and surface by about 30%, while the IR CRE in the atmosphere is in broad agreement. Both sets of results agree that the majority of the negative solar CRE is realized as cooling at the surface and that the atmospheric solar CRE is positive for low-level clouds. However, we diagnose a small positive solar CRE in the atmosphere for all the ISCCP classes, whereas *Chen et al.* [2000] find this quantity to be significantly negative for high clouds and near zero for midlevel clouds. This discrepancy in sign for atmospheric solar CRE can be understood by considering the effect of assuming that all of the optical depth in a high cloud bin exists at the diagnosed cloud top pressure. Such a vertical distribution of condensate in effect shields the lower troposphere from most downwelling solar radiation. In reality, we find that a significant fraction of the total optical depth in an ISCCP high cloud bin would actually be from lower tropospheric clouds. This distribution of condensate not only would allow solar radiation transmitted by the high clouds to pass through the middle and lower tropospheric water vapor, but it also would reflect some fraction of that energy back through the moist layers. This vertical distribution of condensate thereby results in a positive solar CRE.

[36] Given the ambiguity in the definition of cloud type using cloud top pressure and column optical depth, we attempt to investigate the properties and forcing of various cloud types as defined by their geometrical characteristics. Figures 13 and 14 show the properties and radiative effects of several geometrically defined types. As before, the primary differences between the study regions are the relative frequencies of occurrence of the cloud types, with the Southern Ocean tending to have more geometrically thin low clouds (fully half of all layers) and the North Atlantic having more geometrically thin cirrus, with differences on the order of 6%. However, the properties of the layers as well as their radiative effects are statistically indistinguishable between the study regions. This is especially true for the geometrically thin layers and low layers that comprise approximately three fourths of the cloudy layers. We do find that there are statistically significant differences in the IWP

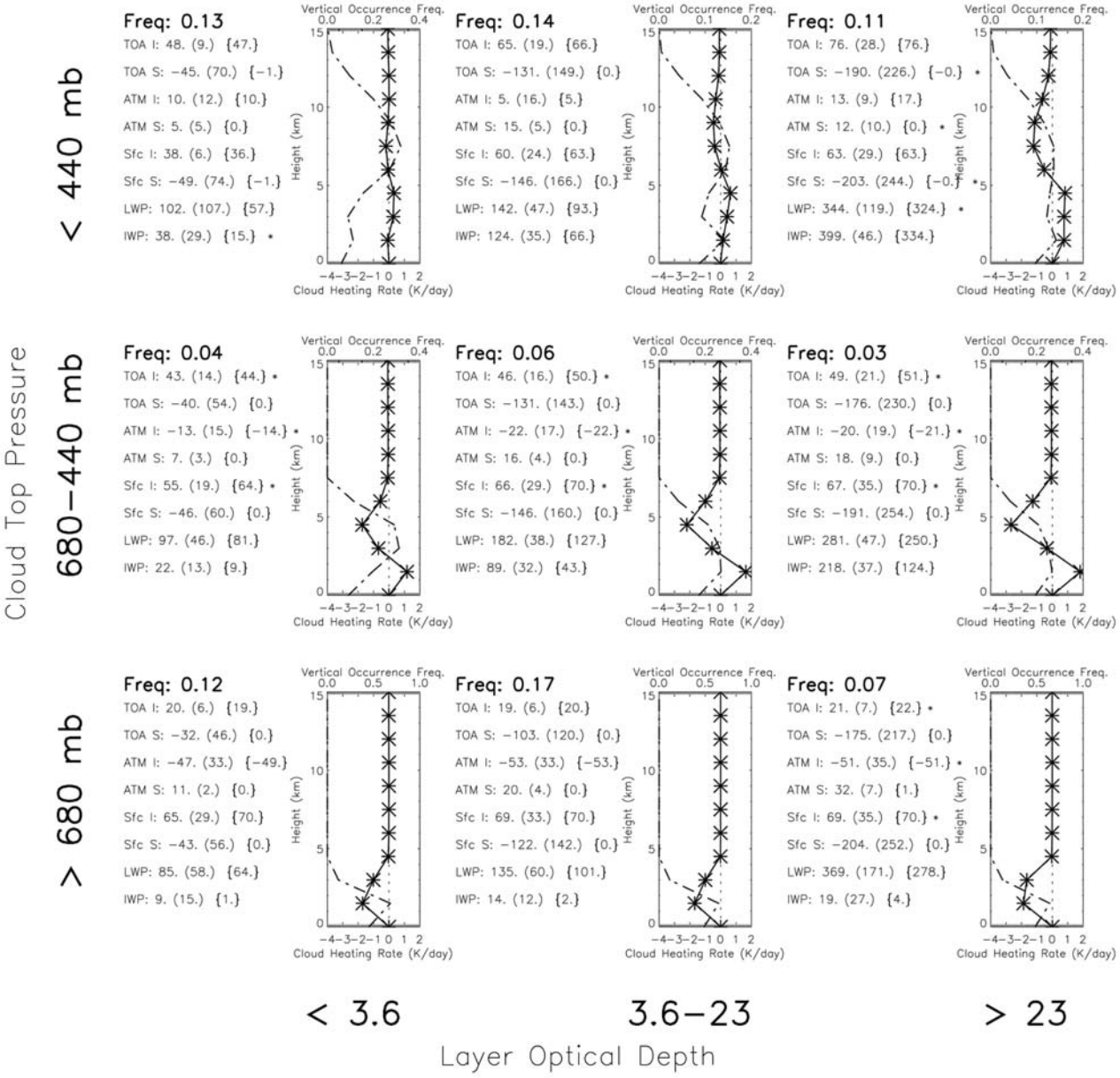

Figure 10. Cloud and radiative statistics compiled from data with layer maximum reflectivity less than +10 dBZ_e collected over the Southern Ocean study region during calendar year 2007. The data are categorized using the standard International Satellite Cloud Climatology Project cloud top pressure-optical depth cloud-type definitions. For each box, the mean, standard deviation (in parentheses), and median values (in curly brackets) of the cloud radiative effects are given (watts per square meter). The graphic in each box shows the net heating rate profile (solid line with symbols), and the vertical occurrence frequency of hydrometeors is shown with the dash-dotted line. ATM, within the atmosphere; I, thermal infrared; IWP, column-integrated ice water path; LWP, column-integrated liquid water path; S, solar radiation averaged over 24 h; Sfc, surface; TOA, top of atmosphere.

and radiative effects of the high-topped deep layers and thick cirrus, although the sample size is small and uncertainties in the derived microphysics are large.

[37] The partitioning of the overall CRE in Figures 8 and 9 can be more clearly understood in light of these geometrically defined cloud types. The most important cloud type from a radiative-forcing perspective in these maritime regions is the shallow boundary layer cloud, which imposes a strong net cooling of approximately 35 W m^{-2} on the atmosphere and a net cooling at the surface of approximately 20 W m^{-2}. This effect, of course, increases for the geometrically thicker clouds, but they occur much less frequently and therefore have less overall radiative impact. Geometrically thin cirrus have near-neutral effect as measured at the TOA, yet this is partitioned between weak solar cooling at the surface and IR warming within the atmosphere. Geometri-

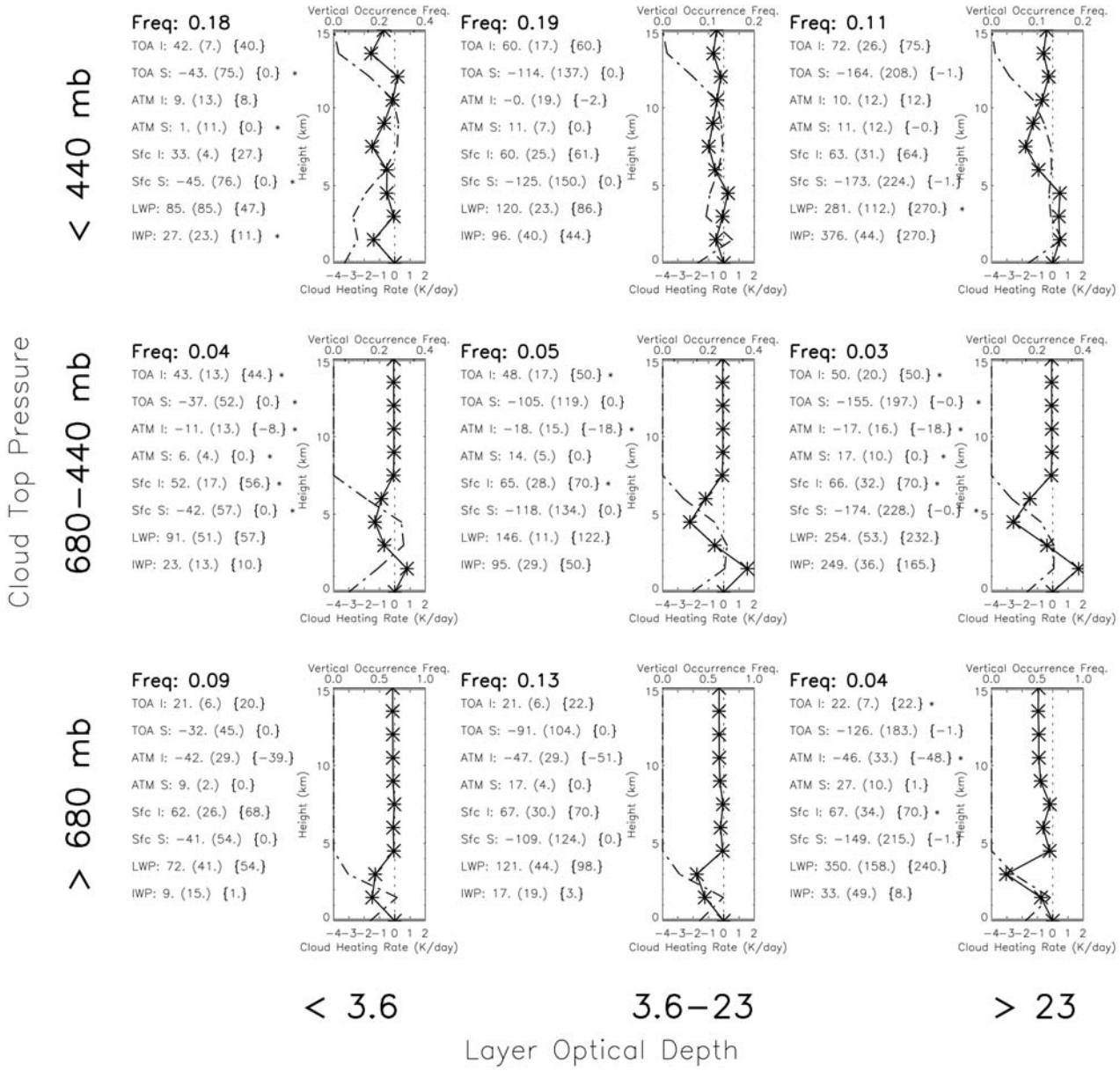

Figure 11. As in Figure 9, except for the North Atlantic study region.

cally thicker clouds tend to have a strong IR warming within the atmosphere and a very strong solar cooling effect at the surface.

5. Summary and Conclusions

[38] The addition of active remote sensors to the A-Train has significantly improved our capacity for inferring cloud properties and associated radiative forcing. Until the advent of these remote-sensing systems, our ability to rigorously diagnose cloud properties was limited to the properties near the cloud top of single-layer cloud systems. Furthermore, because radiative forcing in the atmosphere is such a strong function of cloud vertical structure, our ability to infer critical cloud radiative effects from space has been limited to the effects at TOA. This limitation has left open the question of how the TOA radiative forcing is distributed between the surface and within the atmosphere. This lack of knowledge has resulted in severe ambiguities in characterizing the ability of climate models to simulate the hydrological cycle, further limiting our understanding of cloud feedbacks within a changing climate [e.g., *Dufresne and Bony*, 2008].

[39] We exploit the synergy of these new data streams to infer cloud properties and cloud radiative effects over 20° × 20° latitude-longitude regions situated in the North Atlantic storm tracks and the Southern Ocean (Figure 6). The methodology that we apply is adapted from techniques that we first applied to a similar ground-based data set to examine nearly identical sets of science questions [*Mace et al.*, 2006a, 2006b; *Mace and Benson,* 2008]. In addition to this we implement algorithms designed specifically for the

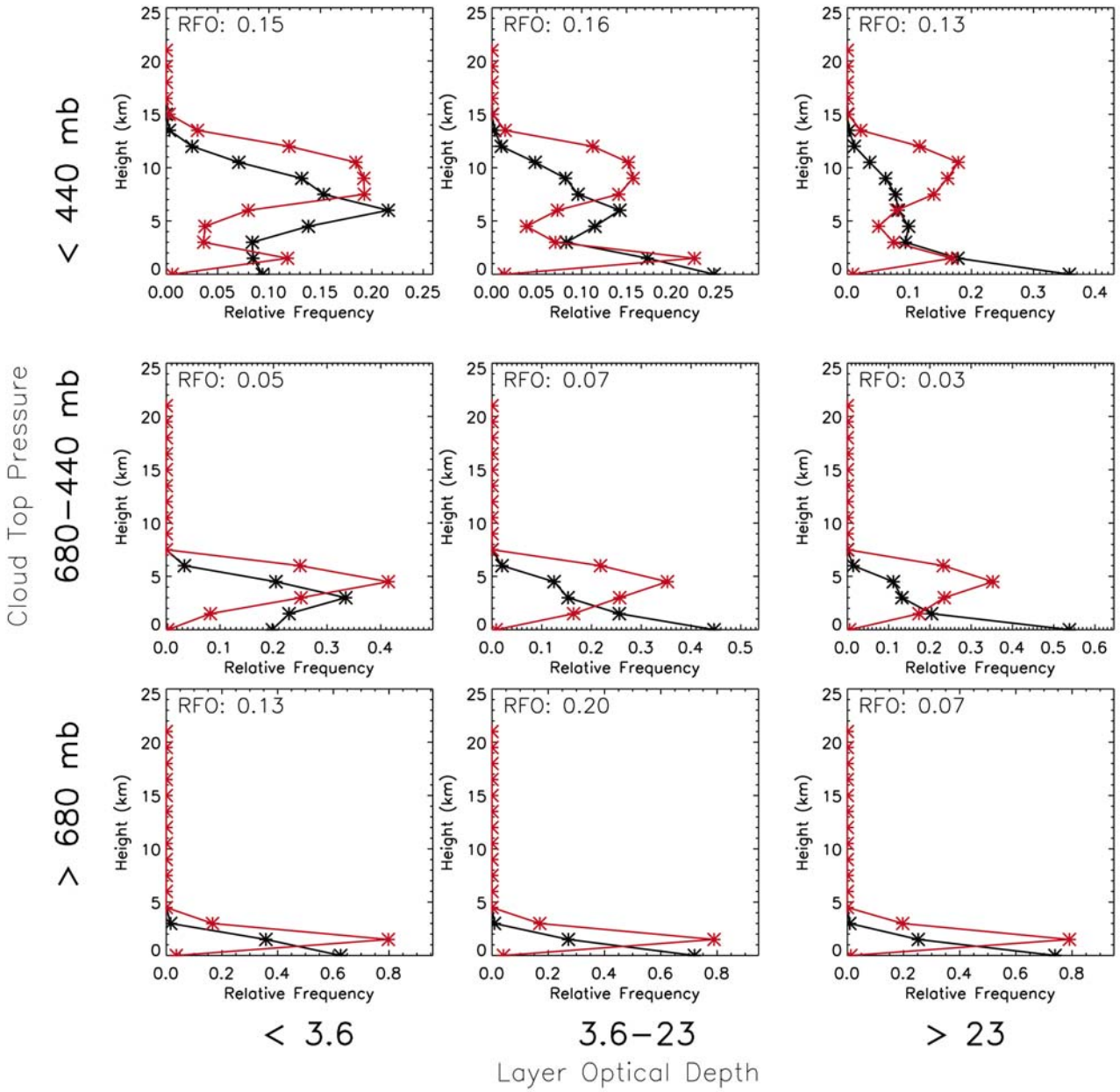

Figure 12. Layer-base (black) and layer-top (red) vertical frequency distributions for cloud top pressure-optical depth classes used by ISCCP. Data presented are from the Southern Ocean study region during 2007 and exclude all profiles with a maximum Z greater than +10 dBZ_e.

A-Train data [*Zhang and Mace*, 2006] (see appendix A) to allow for the possibility of having small- and large-particle modes in the modified gamma distribution for both liquid and ice clouds. The algorithm suite is embedded within an iterative scheme that attempts to minimize the differences with CERES fluxes by adjusting empirical parameters within the retrieval algorithms (appendix B). Using comparisons with in situ data collected during TC4 for ice clouds and from the ARM SGP site for liquid-phase clouds, we determine that uncertainty in IWC and LWC is on the order of 70% and 50%, respectively, and that characteristic errors in IWP and LWP would be on the order of 40% assuming random, uncorrelated, and unbiased error statistics. These assumptions, of course, imply that the error estimates are lower bounds on the actual errors. On the basis of radiative closure and uncertainties in the microphysical retrievals, we further characterize the errors in inferring solar and IR CRE to range between 5 and 10 W m^{-2}, respectively, and the uncertainty in CRH to range between 1 and 2 K day^{-1} for the annual means presented here (appendix C). Comparison of the CRE at the TOA seems to be in overall good agreement with earlier studies. The primary differences are due to the lack of a diurnal cycle in the sun-synchronous A-Train data, causing a high bias in the diurnally averaged solar CRE when compared with data sets that include a full diurnal cycle. We also find differences from earlier studies as to how the TOA

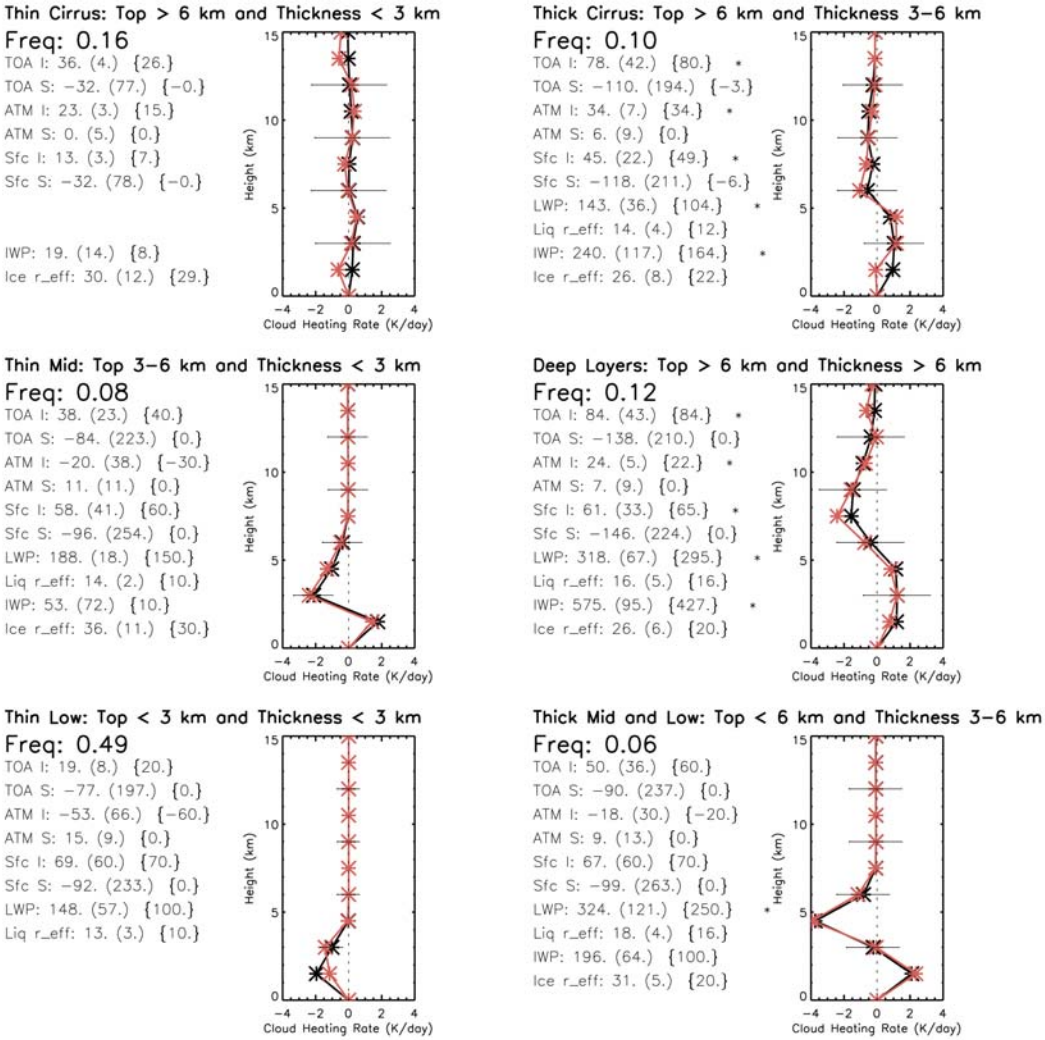

Figure 13. Relative frequency, radiative properties, cloud properties, and net cloud heating profiles for single cloud layers of specified layer top height and geometric thickness. The cloud and radiative properties show the mean value, the standard deviation in parentheses, and the median in curly brackets. Units are watts per square meter, grams per square meter, and micrometers. The net heating profiles compare Southern Ocean (black) with North Atlantic (red). The study period is January–December 2007. Only single-layer cloudy profiles with maximum Z <10 dBZ_e are included. ATM, in atmosphere; I, infrared; S, solar radiation averaged over a 24 h period; Sfc, surface; TOA, top of atmosphere.

radiative effects are distributed between the surface and the atmosphere.

[40] To understand these differences, the cloud and radiative properties over the Southern Ocean and North Atlantic are analyzed in terms of the traditional ISCCP classifications of CTP and τ as well as in terms of geometrically defined cloud types. We find that the standard ISCCP high-cloud classifications are populated not only by high-level layers but also by distinct layers of boundary layer clouds. With nearly identical ice and liquid water paths in these high-cloud bins, as much of the optical opacity used to classify these layers is derived from the boundary layer clouds as from upper tropospheric layers. This ambiguity extends to clouds with middle tropospheric layer-top pressures but to a lesser extent.

[41] The differences between the ISCCP-derived radiative effects and those derived from the A-Train data can be understood in light of these differences in geometric distribution of hydrometeor layers. The IR CRE that we diagnose at TOA and at the surface are larger by approximately 30%, while the atmospheric IR CRE values are similar between the two data sets. Even though ISCCP would bias low the top pressures due to diffuse ice-phase tops, the IR effect should be accurately represented by the passive sensing technique. At the surface, the passive techniques have no information about cloud base and appear to bias low the surface CRE by an amount approximately equal to the differences at TOA. The agreement we find in the atmospheric IR CRE is due to a cancellation of these biases. The solar CRE we diagnose at TOA and surface from the A-Train data is biased high by the lack of diurnal cycle, yet both

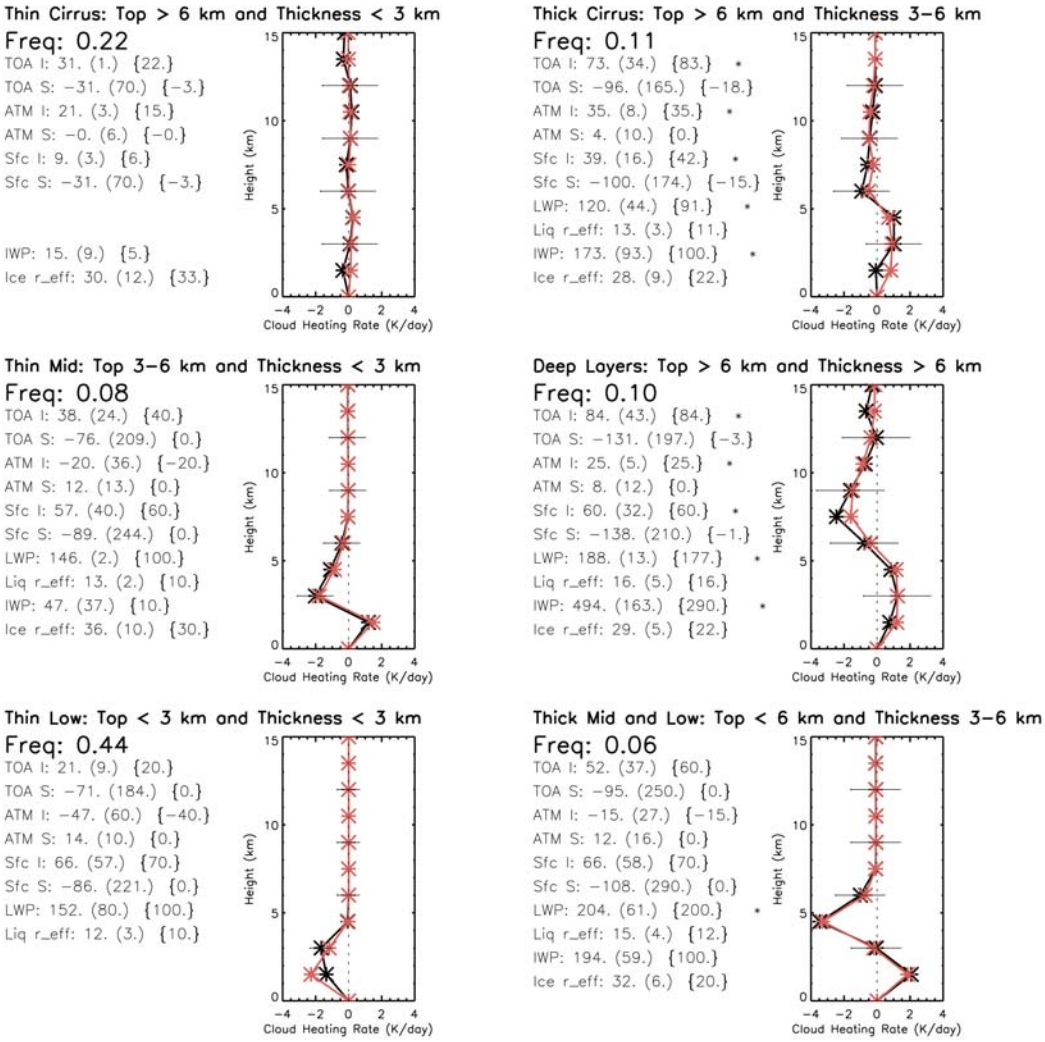

Figure 14. As in Figure 13, except that statistics for the North Atlantic study region are shown and the heating profile in black is for the North Atlantic that in red is for the Southern Ocean.

ISCCP and our results agree that the vast majority of the solar forcing is realized as cooling at the surface. However, the difference in sign in atmospheric CRE is a distinct difference between the data sets for the high- and middle-topped classes and likely arises because of the inability of the passive techniques to represent a vertical distribution of clouds within the classes. For the high clouds, for instance, while the passive technique would place all the optical opacity at the cloud top pressure, in reality cirrus over low-level clouds would result in weak solar heating of the atmosphere due to direct absorption in the liquid clouds and by the reflected sunlight passing twice through the water vapor overlying the reflective lower tropospheric cloud tops. While further study is needed, we conclude that the diagnostic description of the atmosphere created from the A-Train data reasonably represents the occurrence of hydrometeor layers and the radiative influence of those layers on the surface and atmosphere.

[42] The most common and energetically most important cloud types in these maritime regions are boundary layer clouds characterized by geometric thicknesses and cloud tops less than 3 km. This geometrically defined type constitutes approximately one half of all layers observed in these regions and has liquid water paths on the order of 150 g m^{-2} with effective particle radii in the 10–15 μm range. We find that the microphysical properties are statistically indistinguishable between the North Atlantic and Southern Ocean. The low-level clouds impose a strong net cooling effect at the surface driven by solar reflection while also strongly cooling the lower troposphere via IR emission. Net heating of the atmosphere is accomplished by high-level and deeper clouds. These layers demonstrate a strong middle tropospheric heating and upper tropospheric cooling couplet that is dependent on their vertical structure. Geometrically thick cirrus, for instance, actually heat the atmosphere more than deeper frontal layers because the upper tropospheric cooling is largely absent in these semitransmissive layers. In the net, the heating by high clouds largely offsets lower tropospheric cooling by low-level clouds.

[43] Overall, we find that the net TOA cooling effect by clouds at these latitudes arises from a significant partitioning of the radiative forcing between the surface and atmosphere.

The reflective nature of the ubiquitous boundary layer clouds work to maintain the meridional sea surface temperature gradients, while clouds taken as a whole and over an annual average have little net radiative effect on the atmosphere. However, this nearly neutral radiative effect within the atmosphere is the result primarily of strong lower tropospheric cooling by boundary layer clouds coupled with upper tropospheric heating in high-level clouds. Because cloud vertical structure is a property of the dynamic forcing [e.g., *Lau and Crane*, 1995], this atmospheric heating and cooling pattern is superimposed on the large-scale structure of the migratory weather systems at these latitudes, with cooling in regions of cold air advection and heating in regions of warm air advection in such a way as to reinforce their circulations.

Appendix A: The Z-τ Cloud Property Retrieval Algorithm

[44] With radar reflectivity observed by CloudSat and visible optical depth derived from MODIS radiances, our goal is to estimate the properties of a PSD that is consistent with these measurements. The distribution function used by *Delanoe et al.* [2005] is

$$N(D) = N_0 \left(\frac{D}{D_0}\right)^{\alpha} \exp\left(-\left(\frac{D}{D_0}\right)^{\beta}\right), \tag{A1}$$

where D represents the particle diameter for liquid droplets and the maximum dimension for ice crystals, N_0 and D_0 represent characteristic particle concentrations and sizes, respectively, and the exponents α and β determine the relative magnitude and dispersion of the small- and large-particle components of the distribution, respectively. Because we use the radar reflectivity and optical depth as input, we have information regarding large- and small-particle modes, and the algorithm is able to approximately account for the occurrence of bimodality by choosing between physically reasonable combinations of α and β.

[45] An optimal estimation approach [*Rodgers*, 2000] is used as the framework for the inversion of forward model equations. Assuming Rayleigh scattering, we can express the radar reflectivity Z as [*Mace et al.*, 2002]

$$Z = a_Z \int D^{6+b_Z} N(D) dD, \tag{A2}$$

where

$$a_Z = \frac{|K_i|^2}{|K_w|^2} \left(\frac{6}{\pi \rho_{\text{ice}}}\right)^2 a_m^2$$

and $b_Z = 2b_m - 6$ [*Mace et al.*, 2002; *Deng and Mace*, 2006] are empirical parameters that depend on particle habit when considering nonspherical ice crystals as expressed in a mass (m)-dimensional relationship, as by, for instance, *Mitchell* [1996]: $m(D) = a_m D^{b_m}$. Substituting equation (A1) into (A2) and letting $x = D^{\beta}$, we can write

$$Z = \frac{a_Z N_0}{D_0^{\alpha} \beta} \int x^{\frac{b_Z+7+\alpha-\beta}{\beta}} \exp\left(-\frac{x}{D_0^{\beta}}\right) dx. \tag{A3}$$

Equation (A3) can be solved analytically when integrated:

$$Z = \frac{a_Z N_0}{\beta} \Gamma\left(1 + \frac{b_Z + 7 + \alpha - \beta}{\beta}\right) D_0^{b_Z+7}. \tag{A4}$$

An expression for the extinction coefficient can be derived similarly by assuming that the particles are large and the extinction efficiency is twice the particle cross-sectional area ($A(D) = a_A D^{b_A}$):

$$\sigma_{\text{ext}} = \frac{2 a_A N_0}{D_0^{\alpha} \beta} \Gamma\left(1 + \frac{b_A + \alpha + \beta + 1}{\beta}\right) D_0^{b_A+\alpha+1}. \tag{A5}$$

Equations (A4) and (A5) are inverted for N_0 and D_0 using an optimal estimation approach that is nearly identical to that described by *Zhang and Mace* [2006] except that the exponents of the modified gamma distribution and their uncertainties are accounted for in the solution algorithm. *Zhang and Mace* [2006] show that algorithms using radar reflectivity and optical depth have uncertainties in ice water path and particle size on the order of 50% and 30%, respectively. For liquid clouds, the absence of uncertainty in particle habit would cause these error estimates to be upper limits. For ease of reference, we hereafter refer to this approach as the Z-τ algorithm.

[46] Figure A1 shows several example inversions using observational and empirical parameters typical of cirrus and stratocumulus, where a simple shift of empirical relationships and the distribution exponents allows the inversion framework to be applicable to either cloud type. The exponents shown in Figure A1 are the values we use in the iterative algorithm (appendix B). The default values of $\alpha = -1.0$ and $\beta = 3.0$ for cirrus are those found by *Delanoe et al.* [2005] as producing the best agreement with the aircraft data they used in their analysis. The values used for liquid clouds were chosen to provide the best agreement with data collected at the SGP ARM site, where we used input optical depths [*Min and Harrison*, 1996] and layer mean radar reflectivity from the MMCR. Since the algorithm is designed to return a reasonable approximation of the input optical depth, iteration of the distribution exponents and empirical parameters shifts mass between the large- and small-particle modes of the modified gamma distribution, keeping the total cross-sectional area and radar reflectivity approximately constant. This has the effect of modulating the reflected solar flux by shifting scattered sunlight between forward and backward hemispheres through the asymmetry parameter.

[47] In this initial implementation using optical depths derived from MODIS as by *Zhang and Mace* [2006], we apply the algorithm to a layer mean radar reflectivity and extinction coefficient where the layer boundaries are defined from the combined CloudSat and Calipso data. This is particularly an issue in cirrus, where the tops are often below the sensitivity of the CloudSat radar. When applying the algorithm to liquid-phase boundary layer clouds, where the radar becomes unreliable below approximately 1 km and the Calipso lidar is often attenuated, we use the lifting condensation level as derived from collocated European Centre for Medium-Range Weather Forecasts (Reading, England) (ECMWF) data as a reasonable estimate for cloud base.

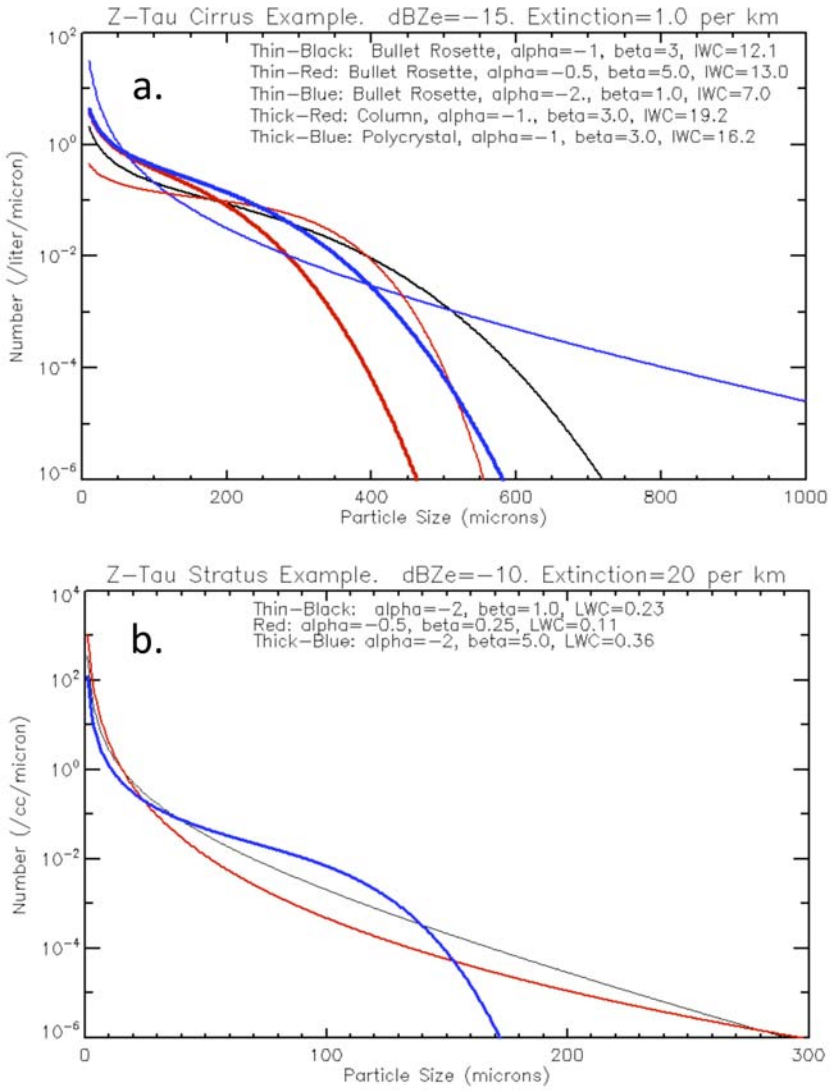

Figure A1. Examples of particle size distributions derived from the modified gamma function in equation (A1). (a) Results based on the ice cloud-like characteristics listed with the various size spectra assumptions and the characteristics of the resulting distributions given. (b) As in Figure A1a, except that liquid clouds are assumed.

[48] Once the layer mean result is obtained, the water paths are distributed through the vertical depth of the layer using a $Z^{0.7}$ weighting for ice clouds [*Protat et al.*, 2007] and a $Z^{0.5}$ weighting for liquid clouds [*Frisch et al.*, 1998] and assuming a constant effective particle size with depth for ice clouds and that the effective radius varies for liquid clouds according to *Dong and Mace* [2003].

Appendix B: Iteration Using Clouds and the Earth's Radiant Energy System Fluxes

[49] The CERES fluxes are used to constrain the retrieval procedure. We consider the set of approximately 15–20 CloudSat footprints that are contained within a CERES footprint and initially scan them for the number of profiles in the set that contain hydrometeor layers. These profiles are then classified based on the properties of the layers and the data that are available (Table 1). We assume that the different profile types within a footprint will interact with the radiation streams in an independent-column-approximation sense and that the CERES flux in the footprint is composed of some linear combination of the fluxes emanating from each of the profile types. So, the profiles of each type are averaged and the retrieval algorithms are applied to the averaged columns to derive the profile of cloud microphysical properties. See appendix A and the text regarding the retrieval algorithms. Once the microphysical properties are estimated, the radiative properties are determined using published radiative parameterizations as described in M06. We use the parameterization of *Slingo* [1989] and *Kiehl et al.* [1998] for the liquid-phase solar and IR, respectively, and that of *Fu* [1996] and *Fu et al.* [1998] for the ice-phase solar and IR. The solar and IR fluxes are calculated using the radiative transfer algorithm of *Toon et al.* [1989] with the *k*-distribution method and correlated-*k* assumption as described by *Kato et al.* [1999, 2001] for the solar spectrum

and by *Mlawer et al.* [1997] for the IR spectrum. The thermodynamic properties of the atmosphere and the surface temperature are given by the ECMWF auxiliary product provided in the CloudSat archive. For surface albedo over ocean we assume a spectrally constant value of 0.05. We neglect aerosol altogether for simplicity.

[50] With the fluxes calculated for each of the column types in the CERES footprint using the default version of the microphysical retrievals, we determine a weighted total flux for the set of profiles by linearly combining the calculated fluxes and their fractional coverage in the footprint: $F_{calc} = \alpha_{clr}F_{clr} + \alpha_{ice}F_{ice} + \alpha_{liq}F_{liq} + \alpha_{mixed}F_{mixed}$, where α is the fractional occurrence of the column type denoted by the subscript and F is the calculated TOA flux for that column type from the initial retrieved microphysics. We are not concerned at this point with whether the calculated fluxes agree with the CERES measurement, but we do keep track of what fraction of the total calculated flux each type contributes; that is, $f_x = F_x/F_{calc}$, where the subscript x refers to the column types. So our goal for the retrieval of each type is to derive a profile of microphysical properties that would produce a TOA flux equal to the fractional amount of the CERES measurement for that column type; that is, $F_x = f_xF_{CERES}$. Once the values of f_x are known within a CERES footprint and we have target values for F_x, we iterate between physically reasonable empirical relations that must be specified within the algorithms or applied to the column in order to determine the column radiative properties. Because of the computational burden, we limit the iterations to a small number of discrete choices. For the Z- τ algorithm, the exponent sets on which we iterate are shown in Figure A1.

[51] We should note that because our goal is to develop a statistical description of the physical properties of hydrometeor occurrence, microphysics, and radiative forcing from the broadest possible set of measurements, the A-Train data set has several peculiarities that require special attention. Foremost among these is that the CALIPSO lidar is able to sense cloud layers that are below the detection threshold of the CloudSat radar. CALIPSO is also able to detect layers that exist below 1 km above the surface, where the CloudSat radar suffers from diminished sensitivity [*Marchand et al.*, 2008; *Mace et al.*, 2007]. When the lidar reports the presence of a cloud layer that is above 1 km and not detected by CloudSat, we know that the reflectivity of the cloudy volumes are less than the detection threshold of the radar (i.e., −31 dBZ_e). So, we specify the radar reflectivity of the layer to be 1 dB less than this minimum value and iterate downward in 2 dB increments using CERES fluxes as a constraint. When a hydrometeor layer exists below the 1 km level according to the lidar that is unobserved by the radar, we simply set the reflectivity to −25 dBZ_e and iterate upward in 5 dBZ_e increments. These procedures are very ad hoc and result in highly uncertain results, but we deem that outcome to be preferable to simply ignoring the layers.

Appendix C: Error Analysis

[52] Error in the results presented in this study arises from many sources, including calibration of the measurements, the applicability of assumptions (i.e., the assumed functional forms of the particle size distributions), the empirical parameters assumed in the retrieval process, and so on. In theory, with the optimal estimation approach we adopt in most of the algorithms, we should be able to evaluate these errors theoretically. However, this theoretical approach requires detailed knowledge of the statistics and covariance of the empirical parameters. In general, these statistics are not known, and we assume, as do others, that the errors and variances are random and uncorrelated. The result of that assumption regarding random and uncorrelated errors is that the aggregate uncertainty decreases as the inverse square root of the number of independent samples. In practice, such an approach results in the average value converging on any systematic bias error. Knowledge of the bias is difficult to obtain and remains largely unknown for most of the quantities discussed in this paper.

[53] *Zhang and Mace* [2006] determined uncertainty in retrieved IWP to be on the order of 40% for a very similar algorithm to the one described in Appendix A. This analysis of uncertainty agreed reasonably well with in situ aircraft measurements presented in that paper. If we use this value of 40% error in IWP and allow for a typical depth of cirrus on the order of 2 km with random uncorrelated errors through the vertical interval, we arrive at an uncertainty in IWC on the order of 100%. This is in broad agreement with our comparison to in situ data collected during TC4 and presented in Table 2 and Figure 3, where we find a 70% RMS difference in retrieved and measured IWC, with an apparent low bias of 18% for these cases. It is unknown whether this bias is a result of incorrect choice of empirical parameters for these cases (i.e., the mass- and area-dimensional relationships) or there is a more fundamental problem with the algorithm. It is also unknown how well these error magnitudes derived from tropical ice clouds can be translated to ice clouds in the middle latitudes. Additional data will be required to ascertain this knowledge. For now, we assume conservatively that our error in IWC for cirrus is approximately a factor of 2, with error in IWP of about 50% for individual profiles. Particle size errors found by Zhang and Mace were on the order of 50% as well.

[54] For liquid-phase clouds, since errors in the mass- and area-dimensional relationships do not exist, we would expect that the water path uncertainty would be smaller than for ice clouds. However, there are other sources of error, not the least of which is the degradation of the CloudSat CPR to sensing clouds below 1 km and the propensity of the CALIPSO lidar to attenuate near cloud top for these layers. Our comparison with ARM data (Figure 4 and Table 2) suggests that the Z-τ algorithm can provide LWP to within 40% when an additional constraint such as CERES fluxes is available over a fairly wide range, although the number of cases is small and the aforementioned problems with the A-Train active sensors are not accounted for in this estimate. Furthermore, the optical depth retrieval from MODIS is likely more uncertain than the optical depth retrieval from MFRSR, suggesting that a 40% uncertainty in LWP is likely a minimal error bound. Comparisons over a range between 10 and 1000 g m^{-2} with AMSR-E and MYD06 retrievals suggest much larger errors, up to a factor of 2 or more (Table 3), although in the range of the mean LWP found for most low-level layers (~150 g m^{-2}) the comparison to the other retrievals is much closer to what we determine from ARM data. We await additional in situ data in maritime

boundary layer clouds to improve on the particle uncertainty estimate of 10% found by *Dong and Mace* [2003].

[55] What we leave unaddressed here due to a lack of data are the uncertainties in water paths and particle sizes in the mixed-phase regimes and precipitating cloud layers. While we attempt to avoid the precipitation problem by filtering profiles above a specified maximum reflectivity, we use an empirical and admittedly ad hoc approach to the mixed-phase problem as described in M06. A multiple linear regression equation is derived by relating radar measurements and temperature to in situ IWC. The liquid phase is estimated by constraining a simple diagnostic parameterization of LWC to AMSR-E LWP. The errors in this procedure are on the order of a factor 2 based on earlier comparisons.

[56] To evaluate the uncertainties in the radiative effect and heating rates we resort to previous studies and the radiative closure we obtain with CERES fluxes. We find that with the iterative scheme described in appendix B, we arrive at an unbiased RMS difference on the order of 20% for TOA IR and solar fluxes (Figure 5). Following the development in *Mace et al.* (2006b), we express the variance in the CRE as $\sigma^2_{\mathrm{CRE}} = (\sigma_{F^2_{\downarrow}} + \sigma_{F^2_{\uparrow}})_{\mathrm{cloudy}} + (\sigma_{F^2_{\downarrow}} + \sigma_{F^2_{\uparrow}})_{\mathrm{clear}}$, where $F\downarrow$ represents downwelling flux (either solar or IR). Assuming that errors in the component fluxes are random and uncorrelated, we can then calculate the error in the mean as the inverse square root of the number of independent samples. We have some idea of the error in the upwelling flux from the CERES measurements (RMS ~40 W m^{-2}), and we assume similar errors in the downwelling fluxes at the surface and assume conservatively that uncertainty in the clear-sky fluxes would be half of what is found in the cloudy sky. Given the variability in the atmosphere, we assume conservatively that samples would fully decorrelate after 100 profiles (approximately 250 km of along-track distance). With approximately 400,000 cloudy profiles in each analysis region, errors in CRE would be on the order of 3 W m^{-2} for all clouds (Table 4). For the CRE quantities shown in Figures 10–14 and the assumption of random uncorrelated errors, the uncertainties would scale as the inverse square root of the number of occurrences of a particular cloud type. For a cloud type with a 10% frequency of occurrence, the uncertainty in CRE would be on the order of 10 W m^{-2}, while for a 50% frequency of occurrence, the uncertainty would be approximately 5 W m^{-2}. These error estimates should be considered lower bounds on the actual uncertainty, given our assumptions. Of particular note is the additional uncertainty in the surface CRE due to the difficulty of determining cloud base in layers that have a propensity to drizzle.

[57] Since the cloud radiative heating is the convergence of net radiant flux into a volume, we approximate the vertical derivative with a simple centered difference formula:

$$H_y = -\frac{1}{\rho c_p}\frac{\partial F_{\mathrm{net},y}}{\partial z} \cong -\frac{1}{\rho c_p}\frac{F_{\mathrm{net},y_{+1}} - F_{\mathrm{net},y_{-1}}}{z_{+1} - z_{-1}},$$

where ρ is the air density, c_p is the specific heat at constant pressure, z is the height, and the subscripts +1 and −1 indicate the vertical levels above and below a level of interest, respectively. We are also primarily interested in the effects of clouds and, therefore, difference H_y in cloudy skies with a calculation that has cloud removed with no other changes to the temperature or moisture profiles. Considering only the first- and second-order terms that would contribute to the uncertainty in H, we can write

$$\sigma^2_{H_y} \cong \frac{1}{\Delta z^2 (\rho c_p)^2}\cdot\left[\left(\sigma^2_{F_{+1,y\uparrow}} + \sigma^2_{F_{+1,y\downarrow}} + \sigma^2_{F_{-1,y\uparrow}} + \sigma^2_{F_{-1,y\downarrow}}\right) + 2\begin{pmatrix}\sigma^2_{F_{-1,y\uparrow}F_{-1,y\downarrow}} + \sigma^2_{F_{-1,y\uparrow}F_{+1,y\uparrow}} + \\ \sigma^2_{F_{-1,y\uparrow}F_{+1,y\downarrow}} + \sigma^2_{F_{-1,y\downarrow}F_{+1,y\uparrow}} + \sigma^2_{F_{-1,y\downarrow}F_{+1,y\downarrow}} + \sigma^2_{F_{+1,y\downarrow}F_{+1,y\uparrow}}\end{pmatrix}\right]$$

with $\Delta z^2 = (z_{+1} - z_{-1})^2$ and terms such as $\sigma^2_{F_{+1,y\uparrow}F_{+1,y\downarrow}}$ representing an error covariance of the indicated fluxes; y is taken to mean either the solar or the IR flux. The terms in the first parenthetical expression are a function of the uncertainties at the layer. The terms in the second parenthetical expression represent error covariances between upwelling and downwelling fluxes and are assumed to be approximately represented by the error covariances of the upwelling and downwelling fluxes at the TOA and surface. With these approximations, we write

$$\sigma^2_H \cong \frac{8}{\Delta z^2 (\rho c_p)^2}\left[\sigma^2_F + r_{\uparrow\downarrow}\sigma^2_F\right],$$

where $r_{\uparrow\downarrow}$ is the correlation coefficient between the different error terms at the boundaries of the layer. In our analysis of the error covariance using ARM data, we find a negative correlation between the downwelling surface radiation flux errors and the upwelling TOA flux errors ($r_{\uparrow\downarrow} = -0.7$ for solar and −0.3 for IR). Note that this analysis corrects several errors in the development presented by *Mace et al.* (2006b). Assuming that the heating rate errors scale also as the inverse square root of the number of independent samples and given the uncertainty in TOA flux, we find heating rate errors to be between 1 and 2 K day^{-1} for the annual means in the analysis regions, depending on the number of independent samples for a specific cloud type. These errors are depicted in the vertical profiles of heating rates in Figures 10, 11, 13, and 14.

[58] **Acknowledgments.** Data from the NASA DC-8 collected during the TC4 experiment were provided by Paul Lawson of SPEC Inc. and Cindy Twohy of Oregon State University. Mark Schoberl and Paul Wenberg were DC-8 mission scientists. I thank them, as well as the rest of the TC4 team (especially Dave Starr and Brian Toon), for their efforts and expertise. Qilong Min of the State University of New York at Albany provided optical depth retrievals from MFRSR data at the ARM site. I would like to acknowledge the efforts of the engineers and scientists at the Jet Propulsion Laboratory, NASA Langley Research Center, Centre National d'Etudes Spatiales (CNES), Ball Aerospace, and the Cooperative Institute for Research in the Atmosphere (CIRA), without whom the CloudSat and CALIPSO projects would not have been successful. Support for this work was provided by NASA through a contract issued by the Jet Propulsion Laboratory, California Institute of Technology, under a contract with NASA. This work was also supported by the NASA Radiation Science Program under grant NNX07AT45G. Data were obtained from the Atmospheric Radiation Measurement Program. An allocation of computer time from the Center for High Performance Computing at the University of Utah is gratefully acknowledged. Sally Benson and Chris Galli at the University of Utah assisted in preparation of data and creation of figures. Their efforts and dedication are gratefully acknowledged.

References

Ackerman, T. P., and G. M. Stokes (2003), The atmospheric radiation measurement program, *Phys. Today*, *56*, 38–45, doi:10.1063/1.1554135.

Austin, R. T., A. J. Heymsfield, and G. L. Stephens (2009), Retrieval of ice cloud microphysical parameters using the CloudSat millimeter-wave ra-

dar and temperature, *J. Geophys. Res.*, *114*, D00A23, doi:10.1029/2008JD010049.
Bony, S., and J.-L. Dufresne (2005), Marine boundary layer clouds at the heart of tropical cloud feedback uncertainties in climate models, *Geophys. Res. Lett.*, *32*, L20806, doi:10.1029/2005GL023851.
Bony, S., J. L. Dufresne, H. Le Treut, J. J. Morcrette, and C. A. Senio (2004), On dynamic and thermodynamics components of cloud changes, *Clim. Dyn.*, *22*, 71–86, doi:10.1007/s00382-003-0369-6.
Bony, S., et al. (2006), How well do we understand and evaluate climate change feedback processes? *J. Clim.*, *19*, 3445–2461, doi:10.1175/JCLI3819.1.
Borg, L. A., and R. Bennartz (2007), Vertical structure of stratiform marine boundary layer clouds and its impact on cloud albedo, *Geophys. Res. Lett.*, *34*, L05807, doi:10.1029/2006GL028713.
Cess, R. D., et al. (1990), Intercomparison and interpretation of climate feedback processes in 19 atmospheric general circulation models, *J. Geophys. Res.*, *95*, 16,601–16,615, doi:10.1029/JD095iD10p16601.
Cess, R. D., et al. (1996), Cloud feedback in atmospheric general circulation models: An update, *J. Geophys. Res.*, *101*, 12,791–12,794, doi:10.1029/96JD00822.
Chen, T., W. B. Rossow, and Y. Zhang (2000), Radiative effects of cloud-type variations, *J. Clim.*, *13*, 264–286, doi:10.1175/1520-0442(2000)013<0264:REOCTV>2.0.CO;2.
Clothiaux, E. E., K. P. Moran, B. E. Martner, T. P. Ackerman, G. G. Mace, T. Uttah, J. H. Mather, K. B. Widener, M. A. Miller, D. J. Rodriguez (1999), The Atmospheric Radiation Measurement program cloud radars: Operational modes, *J. Atmos. Oceanic. Technol.*, *16*, 819-827.
Comstock, J. M., T. P. Ackerman, and G. G. Mace (2002), Ground-based lidar and radar remote sensing of tropical cirrus clouds at Nauru Island: Cloud statistics and radiative impacts, *J. Geophys. Res.*, *107*(D23), 4714, doi:10.1029/2002JD002203.
Delanoe, J., A. Protat, J. Testud, and D. Bouniol (2005), Statistical properties of the normalized ice particle size distribution, *J. Geophys. Res.*, *110*, D10201, doi:10.1029/2004JD005405.
Deng, M., and G. Mace (2006), Cirrus microphysical properties and air motion statistics using cloud radar Doppler moments: Part I. Algorithm description, *J. Appl. Meteorol. Climatol.*, *45*, 1690–1709, doi:10.1175/JAM2433.1.
Dong, X., and G. G. Mace (2003), Profiles of low-level stratus cloud microphysics deduced from ground-based measurements, *J. Atmos. Oceanic Technol.*, *20*, 45–53, doi:10.1175/1520-0426(2003)020<0042:POLLSC>2.0.CO;2.
Dufresne, J.-L., and S. Bony (2008), An Assessment of the primary sources of spread of global warming estimates from coupled atmosphere-ocean models, *J. Clim.*, *21*, 5135–5144, doi:10.1175/2008JCLI2239.1.
Frisch, A. C., G. Feingold, W. Fairall, and T. Uttal (1998), On cloud radar and microwave radiometer measurements of stratus cloud liquid water profiles, *J. Geophys. Res.*, *103*, 23,195–23,197, doi:10.1029/98JD01827.
Fu, Q. (1996), An accurate parameterization of the solar radiative properties of cirrus clouds for climate models, *J. Clim.*, *9*, 2058–2082, doi:10.1175/1520-0442(1996)009<2058:AAPOTS>2.0.CO;2.
Fu, Q., P. Yang, and W. B. Sun (1998), An accurate parameterization of the infrared radiative properties of cirrus clouds for climate models, *J. Clim.*, *9*, 2223–2237, doi:10.1175/1520-0442(1998)011<2223:AAPOTI>2.0.CO;2.
Greenwald, T. J., T. S. L'Ecuyer, and S. A. Christopher (2007), Evaluating specific error characteristics of microwave-derived cloud liquid water products, *Geophys. Res. Lett.*, *34*, L22807, doi:10.1029/2007GL031180.
Im, E., S. L. Durden, and C. Wu (2006), Cloud Profiling Radar for the CloudSat mission, *IEEE Aerosp. Electron. Syst. Mag.*, *20*, 15–18, doi:10.1109/MAES.2005.1581095.
Kato, S., T. P. Ackerman, J. H. Mather, and E. E. Clothiaux (1999), The *k*-distribution method and correlated-*k* approximation for a shortwave radiative transfer model, *J. Quant. Spectrosc. Radiat. Transf.*, *62*, 109–121, doi:10.1016/S0022-4073(98)00075-2.
Kato, S., G. L. Smith, and H. W. Barker (2001), Gamma-weighted discrete ordinate two-stream approximation for computation of domain-averaged solar irradiance, *J. Atmos. Sci.*, *58*, 3797–3803, doi:10.1175/1520-0469(2001)058<3797:GWDOTS>2.0.CO;2.
Kiehl, J., J. Hack, G. B. Bonan, B. A. Boville, D. L. Williamson, and P. J. Rasch (1998), The National Center for Atmospheric Research Community Climate Model: CCM3, *J. Clim.*, *11*, 1131–1149, doi:10.1175/1520-0442(1998)011<1131:TNCFAR>2.0.CO;2.
Kim, D., and V. Ramanathan (2008), Solar radiation budget and radiative forcing due to aerosols and clouds, *J. Geophys. Res.*, *113*, D02203, doi:10.1029/2007JD008434.
Lau, N-C. and M.W. Crane (1995), A satellite view of the synoptic scale organization of cloud properties in midlatitude and tropical cloud systems, *Mon. Wea. Rev.*, *123*, 1984-2006.
Lawson, P. R., and B. A. Baker (2006), Improvement in determination of ice water content from two-dimensional particle imagery: Part I. Image-to-mass relationships, *J. Appl. Meteorol. Climatol.*, *45*, 1282–1290, doi:10.1175/JAM2398.1.
Lawson, P. R., D. O'Connor, P. Zmarzly, K. Weaver, B. Baker, Q. Mo, and H. Jonsson (2006), The 2D-S (stereo) probe: Design and preliminary tests of a new airborne, high-speed, high resolution, particle imaging probe, *J. Atmos. Oceanic Technol.*, *23*, 1462–1477, doi:10.1175/JTECH1927.1.
L'Ecuyer, T. S., N. B. Wood, T. Haladay, G. L. Stephens, and P. W. Stackhouse Jr. (2008), Impact of clouds on atmospheric heating based on the R04 CloudSat fluxes and heating rates data set, *J. Geophys. Res.*, *113*, D00A15, doi:10.1029/2008JD009951.
Mace, G. G., and S. Benson (2008), The vertical distribution of cloud radiative forcing at the SGP ARM Climate Research Facility as revealed by 8-years of continuous data, *J. Clim.*, *21*, 2591–2610, doi:10.1175/2007JCLI1987.1.
Mace, G. G., T. P. Ackerman, P. Minnis and D. F. Young (1998), Cirrus layer microphysical properties derived from surface-based millimeter radar and infrared interferometer data, *J. Geophys. Res.*, *103*, 23,207-23,216.
Mace, G. G., A. J. Heymsfield, and M. R. Poellot (2002), On retrieving the microphysical properties of cirrus clouds using the moments of the millimeter-wavelength Doppler spectrum, *J. Geophys. Res.*, *107*(D24), 4815, doi:10.1029/2001JD001308.
Mace, G. G., Y. Zhang, S. Platnick, M. D. King, P. Minnis, and P. Yang (2005), Evaluation of cirrus cloud properties from MODIS radiances using cloud properties derived from ground-based data collected at the ARM SGP site, *J. Appl. Meteorol.*, *44*, 221–240.
Mace, G. G., et al. (2006a), Cloud radiative heating at the ARM Climate Research Facility: Part 1. Technique, validation, and comparison to satellite-derived diagnostic quantities, *J. Geophys. Res.*, *111*, D11S90, doi:10.1029/2005JD005921.
Mace, G. G., S. Benson, and S. Kato (2006b), Cloud radiative heating at the ARM Climate Research Facility: Part 2. The vertical redistribution of radiant energy by clouds, *J. Geophys. Res.*, *111*, D11S91, doi:10.1029/2005JD005922.
Mace, G. G., R. Marchand, Q. Zhang, and G. Stephens (2007), Global hydrometeor occurrence as observed by CloudSat: Initial observations from summer 2006, *Geophys. Res. Lett.*, *34*, L09808, doi:10.1029/2006GL029017.
Mace, G. G., Q. Zhang, M. Vaughan, R. Marchand, G. Stephens, C. Trepte, and D. Winker (2009), A description of hydrometeor layer occurrence statistics derived from the first year of merged CloudSat and CALIPSO data, *J. Geophys. Res.*, *114*, D00A26, doi:10.1029/2007JD009755.
Marchand, R. T., G. G. Mace, and T. P. Ackerman (2008), Hydrometeor detection using CloudSat, an Earth orbiting 94 GHz cloud radar, *J. Atmos. Oceanic Technol.*, *25*, 531–546, doi:10.1175/2007JTECHA1006.1.
Matrosov, S. Y., M. D. Shupe, A. J. Heymsfield, and P. Zuidema (2003), Ice cloud optical thickness and extinction estimates from radar measurements, *J. Appl. Meteorol.*, *42*, 1584–1597, doi:10.1175/1520-0450(2003)042<1584:ICOTAE>2.0.CO;2.
Min, Q.-L., and L. C. Harrison (1996), Cloud properties derived from surface MFRSR measurements and comparison with GOES results at the ARM SGP site, *Geophys. Res. Lett.*, *23*, 1641, doi:10.1029/96GL01488.
Mitchell, D. L. (1996), Use of mass- and area-dimensional power laws for determining precipitation particle terminal velocities, *J. Atmos. Sci.*, *53*, 1710–1723, doi:10.1175/1520-0469(1996)053<1710:UOMAAD>2.0.CO;2.
Mlawer, E. J., S. J. Taubman, P. D. Brown, M. J. Iacono, and S. A. Clough (1997), Radiative transfer for inhomogeneous atmospheres: RRTM, a validated correlated-*k* model for the longwave, *J. Geophys. Res.*, *102*, 16,663–16,682, doi:10.1029/97JD00237.
Norris, J. R., and S. F. Iacobellis (2005), North Pacific cloud feedbacks inferred from synoptic-scale dynamic and thermodynamic relationships, *J. Clim.*, *18*, 4862–4879, doi:10.1175/JCLI3558.1.
Ockert-Bell, M. E., and D. L. Hartmann (1992), The effect of cloud type on earth's energy balance: Results for selected regions. *J. Clim.*, *5*, 1157–1171.
O'Dell, C. W., F. J. Wentz, and R. Bennartz (2008), Cloud liquid water path from satellite-based passive microwave observations: A new climatology over the global oceans, *J. Clim.*, *21*, 1721–1739, doi:10.1175/2007JCLI1958.1.
Platnick, S., M. D. King, S. A. Ackerman, W. P. Menzel, B. A. Baum, J. C. Riedi, and R. A. Frey (2003), The MODIS cloud products: Algorithms and examples from Terra, *IEEE Trans. Geosci. Remote Sens.*, *41*(2), 459–473, doi:10.1109/TGRS.2002.808301.

Polonsky, I. N., L. C. Labonnote, and S. Cooper (2008), Level 2 cloud optical depth product process description and interface control document, Coop. Inst. for Res. in the Atmos., Colorado State Univ., Fort Collins.

Potter, G. L., and R. D. Cess (2004), Testing the impact of clouds on the radiation budgets of 19 atmospheric general circulation models, *J. Geophys. Res.*, *109*, D02106, doi:10.1029/2003JD004018.

Protat, A., J. Delanoe, D. Bouniol, A. J. Heymsfield, A. Bansemer, and P. Brown (2007), Evaluation of ice water content retrievals from cloud radar reflectivity and temperature using a large airborne in situ microphysical database, *J. Appl. Meteorol. Climatol.*, *46*, 557–572, doi:10.1175/JAM2488.1.

Ramanathan, V. (1987), The role of Earth radiation budget studies in climate and general circulation research, *J. Geophys. Res.*, *92*, 4075–4095, doi:10.1029/JD092iD04p04075.

Rodgers, C. D. (2000), *Inverse Methods for Atmospheric Sounding: Theory and Practice*, World Sci., Singapore.

Rossow, W. B., and R. A. Schiffer (1999), Advances in understanding clouds from ISCCP, *Bull. Am. Meteorol. Soc.*, *80*, 2261–2288, doi:10.1175/1520-0477(1999)080<2261:AIUCFI>2.0.CO;2.

Rossow, W. B., and T.-C. Zhang (1995), Calculation of surface and top of atmosphere radiative fluxes from physical quantities based on ISCCP data sets 2: Validation and first results, *J. Geophys. Res.*, *100*, 1167–1197, doi:10.1029/94JD02746.

Sanderson, B. M., C. Piani, W. J. Ingram, D. A. Stone, and M. R. Allen (2008), Towards constraining climate sensitivity by linear analysis of feedback patterns in thousands of perturbed-physics GCM simulations, *Clim. Dyn.*, *30*, 175–19, doi:10.1007/s00382-007-0280-7.

Senior, C. A., and J. F. B. Mitchell (1993), Carbon dioxide and climate: The impact of cloud parameterization, *J. Clim.*, *6*, 393–416, doi:10.1175/1520-0442(1993)006<0393:CDACTI>2.0.CO;2.

Slingo, J. M. (1989), A GCM parameterization for the shortwave radiative properties of water clouds, *J. Atmos. Sci.*, *46*, 1419–1427, doi:10.1175/1520-0469(1989)046<1419:AGPFTS>2.0.CO;2.

Soden, B. J., and I. M. Held (2006), An assessment of climate feedbacks in coupled ocean-atmosphere models, *J. Clim.*, *19*, 3354–3360, doi:10.1175/JCLI3799.1.

Stephens, G. L. (2005), Cloud feedbacks in the climate system: A critical review, *J. Atmos. Sci.*, *18*, 237–273.

Stephens, G. L., et al. (2002), The CloudSat mission and the A-Train, *Bull. AMS*, *83*, 1771–1790, doi:10.1175/BAMS-83-12-1771.

Toon, O. B., C. P. McKay, T. P. Ackerman, and K. Santhanam (1989), Rapid calculation of radiative heating rates and photodissociation rates in inhomogeneous multiple scattering atmospheres, *J. Geophys. Res.*, *94*(D13), 16,287–16,301, doi:10.1029/JD094iD13p16287.

Twohy, C. H., A. J. Schanot, and W. A. Cooper (1997), Measurement of condensed water content in liquid and ice clouds using an airborne counterflow virtual impactor, *J. Atmos. Oceanic Technol.*, *14*, 197–202, doi:10.1175/1520-0426(1997)014<0197:MOCWCI>2.0.CO;2.

Vaughan, M., S. Young, D. Winker, K. Powell, A. Omar, Z. Liu, Y. Hu, and C. Hostetler (2004), Fully automated analysis of space-based lidar data: An overview of the CALIPSO retrieval algorithms and data products, *Proc. SPIE Int. Soc. Opt. Eng.*, *5575*, 16–30.

Weaver, C. P. (2003), Efficiency of storm tracks an important climate parameter? The role of cloud radiative heating in poleward heat transport, *J. Geophys. Res.*, *108*(D1), 4018, doi:10.1029/2002JD002756.

Webster, P. J., and G. L. Stephens (1981), Clouds and climate: Sensitivity of simple systems, *J. Atmos. Sci.*, *38*, 235–247, doi:10.1175/1520-0469(1981)038<0235:CACSOS>2.0.CO;2.

Wentz, F. J., and T. Meissner (2000), AMSR algorithm theoretical basis document, version 2, Remote Sens. Syst., Santa Rosa, Calif.

Wielicki, B. (2001), New generation of CERES radiation budget data available, *Earth Observer*, *13*, 23–24.

Wielicki, B. A., et al. (1998), Clouds and the Earth's radiant energy system (CERES): Algorithm overview, *IEEE Trans. Geosci. Remote Sens.*, *36*(4), 1127–1141.

Wilcoxon, F. (1945), Individual comparisons by ranking methods, *Biometrics Bull.*, *1*, 80–83, doi:10.2307/3001968.

Williams, K. D., and G. Tselioudis (2007), GCM intercomparison of global cloud regimes: Present-day evaluation and climate change response, *Clim. Dyn.*, *29*, 231–250, doi:10.1007/s00382-007-0232-2.

Winker, D. M., B. H. Hunt, and M. J. McGill (2007), Initial performance assessment of CALIOP, *Geophys. Res. Lett.*, *34*, L19803, doi:10.1029/2007GL030135.

Wood, R., and D. L. Hartmann (2006), Spatial variability of liquid water path in marine low cloud: The importance of mesoscale cellular convection, *J. Clim.*, *19*, 1748–1765, doi:10.1175/JCLI3702.1.

Zhang, M. H., et al. (2005), Comparing clouds and their seasonal variations in 10 atmospheric general circulation models with satellite measurements, *J. Geophys. Res.*, *110*, D15S02, doi:10.1029/2004JD005021.

Zhang, Y., and G. Mace (2006), Retrieval of cirrus microphysical properties with a suite of algorithms for airborne and spaceborne lidar, radar, and radiometer data, *J. Appl. Meteorol. Climatol.*, *45*, 1665–1689, doi:10.1175/JAM2427.1.

Zhang, Y. C., and W. B. Rossow (1997), Estimating meridional energy transports by the atmospheric and oceanic general circulations using boundary fluxes, *J. Clim.*, *10*, 2358-2374.

Zhang, Y. C., W. B. Rossow, and A. A. Lacis (1995), Calculation of surface and top of atmosphere radiative fluxes from physical quantities based on ISCCP data sets: Part 1. Method and sensitivity to input data uncertainties, *J. Geophys. Res.*, *100*, 1149–1165, doi:10.1029/94JD02747.

G. G. Mace, Department of Atmospheric Science, University of Utah, Salt Lake City, UT 84112, USA. (Jay.Mace@utah.edu)